



ALMA CYCLE 1 OBSERVATIONS OF THE HH46/47 MOLECULAR OUTFLOW: STRUCTURE, ENTRAINMENT, AND CORE IMPACT

YICHEN ZHANG^{1,2}, HÉCTOR G. ARCE², DIEGO MARDONES¹, SYLVIE CABRIT^{3,4}, MICHAEL M. DUNHAM⁵, GUIDO GARAY¹, ALBERTO NORIEGA-CRESPO⁶, STELLA S. R. OFFNER⁷, ALEJANDRO C. RAGA⁸, AND STUART A. CORDER⁹

¹ Departamento de Astronomía, Universidad de Chile, Casilla 36-D, Santiago, Chile; yczhang.astro@gmail.com

² Astronomy Department, Yale University, P.O. Box 208101, New Haven, CT 06520, USA

³ LERMA, Observatoire de Paris, UMR 8112 du CNRS, ENS, UPMC, UCP, 61 Av. de l'Observatoire, F-75014 Paris, France

⁴ Institut de Planétologie et d'Astrophysique de Grenoble (IPAG) UMR 5274, Grenoble, F-38041, France

⁵ Harvard-Smithsonian Center for Astrophysics, 60 Garden Street, Cambridge, MA 02138, USA

⁶ Space Telescope Science Institute, 3700 San Martin Dr., Baltimore, MD 21218, USA

⁷ Department of Astronomy, University of Massachusetts, Amherst, MA 01002, USA

⁸ Instituto de Ciencias Nucleares, UNAM, Ap. 70-543, 04510 D.F., Mexico

⁹ Joint ALMA Observatory, Av. Alonso de Córdova 3107, Vitacura, Santiago, Chile

Received 2016 January 31; revised 2016 June 20; accepted 2016 July 6; published 2016 November 29

ABSTRACT

We present Atacama Large Millimeter/sub-millimeter Array Cycle 1 observations of the HH 46/47 molecular outflow using combined 12 m array and Atacama Compact Array observations. The improved angular resolution and sensitivity of our multi-line maps reveal structures that help us study the entrainment process in much more detail and allow us to obtain more precise estimates of outflow properties than in previous observations. We use ^{13}CO (1–0) and C^{18}O (1–0) emission to correct for the ^{12}CO (1–0) optical depth to accurately estimate the outflow mass, momentum, and kinetic energy. This correction increases the estimates of the mass, momentum, and kinetic energy by factors of about 9, 5, and 2, respectively, with respect to estimates assuming optically thin emission. The new ^{13}CO and C^{18}O data also allow us to trace denser and slower outflow material than that traced by the ^{12}CO maps, and they reveal an outflow cavity wall at very low velocities (as low as 0.2 km s^{-1} with respect to the core's central velocity). Adding the slower material traced only by ^{13}CO and C^{18}O , there is another factor of three increase in the mass estimate and 50% increase in the momentum estimate. The estimated outflow properties indicate that the outflow is capable of dispersing the parent core within the typical lifetime of the embedded phase of a low-mass protostar and that it is responsible for a core-to-star efficiency of 1/4 to 1/3. We find that the outflow cavity wall is composed of multiple shells associated with a series of jet bow-shock events. Within about 3000 au of the protostar the ^{13}CO and C^{18}O emission trace a circumstellar envelope with both rotation and infall motions, which we compare with a simple analytic model. The CS (2–1) emission reveals tentative evidence of a slowly moving rotating outflow, which we suggest is entrained not only poloidally but also toroidally by a disk wind that is launched from relatively large radii from the source.

Key words: Herbig–Haro objects – ISM: clouds – ISM: individual objects (HH 46, HH 47) – jets and outflows – stars: formation

1. INTRODUCTION

Outflows play an important role in star formation and the evolution of molecular clouds and cores. They carve out cavities in their parent cores and inject energy and momentum into the star-forming environment. They may be responsible for dispersing the core (Arce & Sargent 2006), terminating the infall phase (e.g., Velusamy & Langer 1998), and thereby determining the final stellar mass and the core-to-star efficiency (e.g., Matzner & McKee 2000; Myers 2008; Offner & Arce 2014). In particular, a nearly constant 30% efficiency due to outflows would be one explanation for the similar shape of the core mass function (CMF) and the initial mass function (IMF) (e.g., Alves et al. 2007; Offner et al. 2014). However, it is still unclear whether the outflow is powerful enough to disperse 70% of the gas in the surrounding core. While some studies have shown that outflows have a profound effect on the environment surrounding the protostar and are able to disperse the parent core on timescales less than 1 Myr (e.g., Tafalla & Myers 1997; Fuller & Ladd 2002; Arce & Sargent 2006), other studies have claimed that the mass-loss rate from the outflows is too low and outflows cannot be the sole agent responsible for core dispersal (e.g., Hatchell et al. 2007; Curtis et al. 2010).

More studies with reliable estimates of the outflow mass, momentum, and energy are needed to solve this discrepancy. Considering that the denser material at low velocities, which is untraceable by optically thick ^{12}CO emission, may contribute a large fraction of the outflow mass, optically thinner tracers like ^{13}CO and C^{18}O are needed to understand the impact of the outflow on the denser material (Arce & Sargent 2006).

The accretion of material from the circumstellar disk onto the protostar drives bipolar magneto-centrifugal winds. A collimated wind or the collimated portion of a wind, which is typically observed in atomic lines, is usually referred to as a jet. The molecular outflow is believed to be the ambient gas entrained by such bipolar winds. The entrainment process is not yet clearly understood. Models include entrainment through wide-angle winds (e.g., Li & Shu 1996) and jet bow shocks (internal and/or leading) (e.g., Raga & Cabrit 1993). In the wide-angle wind entrainment model, a radial wind blows into the ambient material, forming a thin outflowing shell. In the jet bow-shock entrainment model, a jet propagates into the ambient material and forms bow shocks which accelerate the ambient gas producing outflow shells surrounding the jet. These two mechanisms may co-exist but one may play a more

important role than the other depending on the distribution of the ambient material.

This paper is a follow-up study of the HH 46/47 molecular outflow (Arce et al. 2013, Paper I hereafter), using Atacama Large Millimeter/sub-millimeter Array (ALMA) Cycle 1 observations. The HH 46/47 outflow is driven by a low-mass early Class I protostar (HH 47 IRS, HH 46 IRS 1, IRAS 08242-5050, $12 L_\odot$) which resides in the Bok globule ESO 216-6A, located on the outskirts of the Gum Nebula at a distance of 450 pc (Schwartz 1977; Reipurth 2000; Noriega-Crespo et al. 2004). *Hubble Space Telescope* (*HST*) observations indicate that HH 47 IRS is a binary system with an observed separation between the two components of the system of $0''.26$ or about 120 au (Reipurth 2000). As the driving source lies very close to the edge of the globule, the blueshifted outflow can be seen at optical wavelengths extending outside of the globule, while most of the redshifted outflow lies inside of the globule and therefore is best seen in infrared. Wide-field, narrowband H α and [S II] optical images by Stanke et al. (1999) revealed that the jet may extend further away from the globule, extending 2.6 pc on the plane of the sky. The HH 46/47 outflow has been extensively studied in optical and infrared. Studies combining the optical spectral data and proper motion observations estimated the average jet velocity to be 300 km s^{-1} and the inclination between the jet and the plane of the sky to be about 30° – 40° (Reipurth 1989; Reipurth & Heathcote 1991; Eislöffel & Mundt 1994; Micono et al. 1998; Hartigan et al. 2005). In addition, the infrared shocked H $_2$ emission also shows an outflow cavity structure with a width of $36''$ and a length of about $2'$ (Eislöffel et al. 1994; Noriega-Crespo et al. 2004).

The HH 46/47 molecular outflow was recently observed in ^{12}CO (1–0) by ALMA in Cycle 0 (Paper I). The molecular outflow appears to be highly asymmetric: the blueshifted lobe extends no more than $30''$, while the redshifted lobe extends about $2'$. Detailed analysis of the morphology and kinematics of the molecular outflow showed evidence of wide-angle wind entrainment for the blueshifted outflow and jet bow-shock entrainment for the redshifted outflow. These asymmetries are due to the fact that the blueshifted jet is mostly outside of the globule where there is little or no molecular gas for it to entrain, while the redshifted jet plunges into the parent cloud. *APEX* and *Herschel* observations revealed the existence of warm CO, H $_2$ O, OH, and [O I] emission in this outflow, produced by shocks where the protostellar jet/wind interacts with the parent core (van Kempen et al. 2009, 2010; Wampfler et al. 2010).

Here we present analysis of an ALMA Cycle 1 observation of ^{12}CO (1–0), ^{13}CO (1–0), C^{18}O (1–0), CS (2–1), and other molecules using the ALMA 12 m array and Atacama Compact Array (ACA). Molecules such as ^{13}CO and C^{18}O trace higher column density gas than ^{12}CO , allowing us to obtain a more accurate assessment of the outflow's impact on the core. We also use ^{13}CO and C^{18}O to correct the CO opacity to more accurately determine the properties of the outflow. Compared with previous ALMA observations, the new ^{12}CO data also have improved angular resolution and sensitivity to large structures and reveal richer details of the outflow that help constrain the outflow entrainment mechanism.

2. OBSERVATIONS

The observations were carried out using ALMA from 2013 November 5 to 2015 April 11. Two different correlator

configurations were used to provide images on six molecular lines and two 2 GHz wide continuum bands in Band 3. Data from both the 12 m array and the ACA (including the 7 m array and the 12 m total power dishes) were obtained.

With the first correlator configuration, ^{12}CO (1–0) at 115.27 GHz and C^{17}O (1–0) at 112.36 GHz were observed along with continuum emission at 100.7 and 102.7 GHz (3 mm). The ^{12}CO line was observed with a channel width of 61 kHz (0.2 km s^{-1}) over a 117.2 MHz (305 km s^{-1}) bandwidth, and the C^{17}O line was observed with a channel width of 30.5 kHz (0.1 km s^{-1}) over a 58.6 MHz bandwidth (152 km s^{-1}). The continuum emission was observed with two 1875 MHz wide bands. The 12 m array data were obtained over 3 scheduling blocks, with 32–37 antennas, and projected baselines in the range of 12–528 m. A rectangular 23 point mosaic with contiguous pointings separated by $25''.8$ and oriented at a position angle (P.A.) of about 60° was used to map the outflow. The 7 m array data were obtained over 10 scheduling blocks, with 8–10 antennas, and projected baselines in the range of 7–44 m. A 9 point mosaic with a pointing separation of $44''.2$ was used for mapping. The total power data were obtained over 18 scheduling blocks, with a mapping area of $6' \times 3.8'$. The resultant map combining the 12 m array, 7 m array, and total power data has a size of about $2'1 \times 1'05$ and is centered at $8^{\text{h}}25^{\text{m}}40^{\text{s}}$, $-51^{\circ}00'59''$ (J2000).

The second correlator configuration provides simultaneous observations of ^{13}CO (1–0) at 110.2 GHz, C^{18}O (1–0) at 109.78 GHz, CS (2–1) at 97.98 GHz, and C^{34}S (2–1) at 96.41 GHz. Each line was observed with a channel width of 30.5 kHz (0.1 km s^{-1}) and over a bandwidth of 58.6 MHz (160 km s^{-1}). The 12 m array data were obtained over 3 scheduling blocks, with 29 antennas, and projected baselines ranging from 12 to 340 m. A 26 point mosaic with pointings separated by $27''$ was used to cover a similar but slightly wider area than the ^{12}CO data. The 7 m array data were obtained over 10 scheduling blocks, with 8–10 antennas, and projected baselines ranging from 7 to 44 m. A 7 point mosaic with a pointing separation of $46''.3$ was used. The total power data were obtained over 12 scheduling blocks, with a mapping area of $6' \times 4.2'$. The resultant combined map is about $2' \times 1.3'$, centered at $8^{\text{h}}25^{\text{m}}40^{\text{s}}$, $-51^{\circ}00'57''$ (J2000).

Ganymede, Pallas, J0538-440, Jupiter, Mars, Callisto, and J1256-0547 were used as gain and flux calibrators; J0845-5448 and J0701-4634 were used as phase calibrators; and J0747-3310, J0922-3959, J0538-4405, J1107-4449, J1037-2934, and J0519-4546 were used as bandpass calibrators. The data were edited, calibrated, and imaged in CASA. The 12 m array and the 7 m array visibilities were combined with their weighting factors estimated from the data noise using the CASA task *statwt*. The combined interferometric data have projected baselines ranging from 7 to 525 m for ^{12}CO and C^{17}O , and baselines ranging from 7 to 340 m for ^{13}CO , C^{18}O , CS, and C^{34}S . The data were imaged using the CLEAN algorithm. For the spectral data we defined a different clean region for each channel, encircling the area with the brightest emission. Robust weighting with the robust parameter of 0.5 is used in the clean process. The resulting synthesized beam is $1''.3 \times 1''.3$ for the ^{12}CO data cube and $3''.2 \times 1''.6$ for the ^{13}CO and C^{18}O data cubes.

The interferometric data and the total power data were then combined in the image space using the CASA task *feather*. In the rest of the paper, if not indicated otherwise, we will show

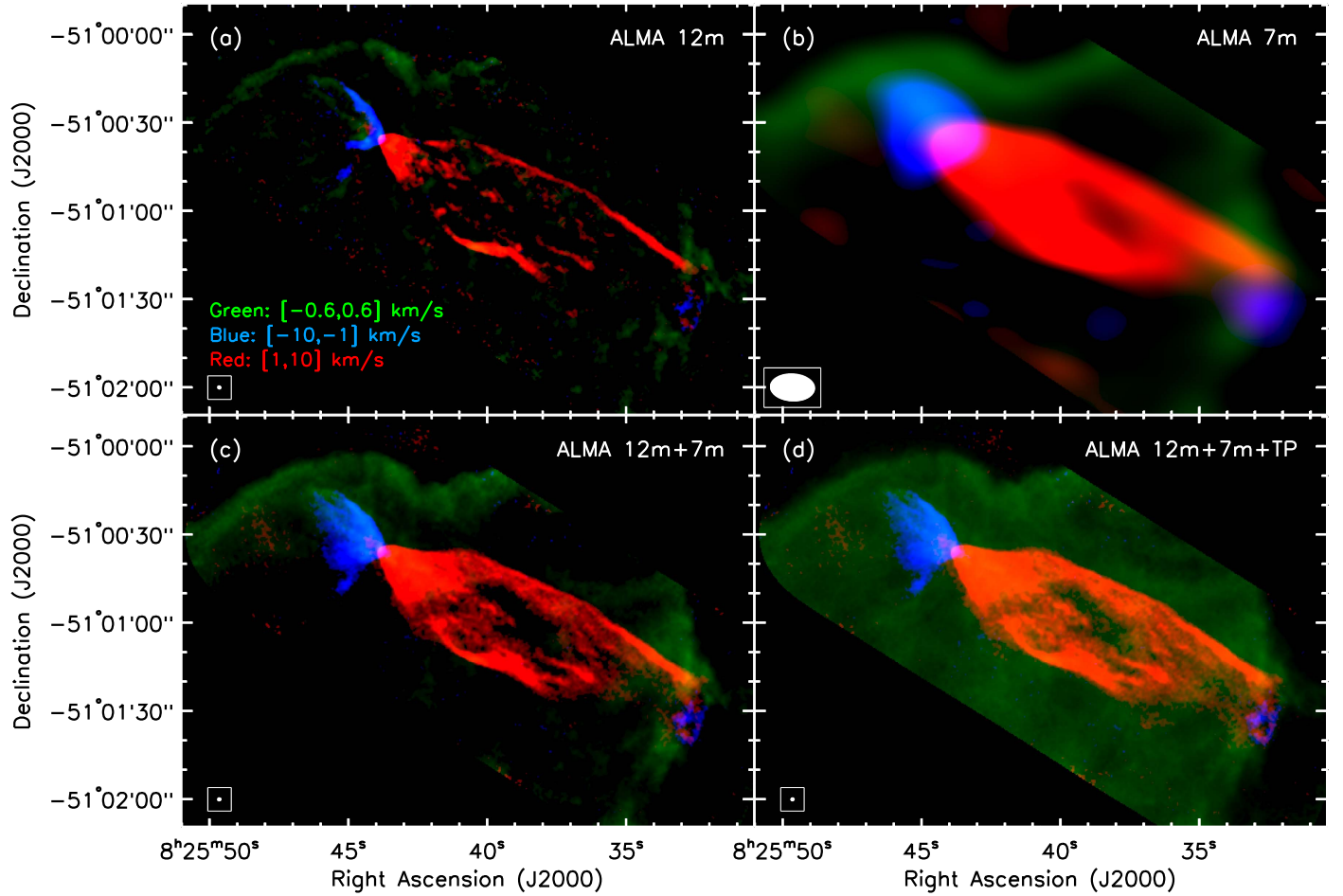


Figure 1. Three-color images showing ^{12}CO (1–0) integrated emission from (a) the 12 m array data, (b) the 7 m array data, (c) the interferometric data combining the 12 m array and 7 m array, and (d) the combined data of the interferometric data and total power data. The red, green, and blue color scales show emission integrated over the velocity ranges from 1 to 10 km s^{-1} , from -0.6 to 0.6 km s^{-1} and from -10 to -1 km s^{-1} (relative to the cloud velocity), respectively. From panel (a) to (d), the synthesized beams are $1.^{\prime\prime}33 \times 1.^{\prime\prime}28$ (P.A. = -59.7°), $1.^{\prime\prime}.3 \times 9.^{\prime\prime}.4$ (P.A. = 86.8°), $1.^{\prime\prime}.37 \times 1.^{\prime\prime}.31$ (P.A. = -58.2°), and $1.^{\prime\prime}.37 \times 1.^{\prime\prime}.31$ (P.A. = -58.2°) respectively (the white ellipse in the lower-left corner of each panel).

the combined data. Figure 1 shows the ^{12}CO (1–0) integrated maps as an example of the combination. With an angular resolution similar to the 12 m array data, the combined data keep the detailed structures revealed by the 12 m array data, while also showing the diffuse emission around the cloud velocity. Details of the ^{12}CO emission will be discussed in Section 3.2. Throughout the paper we define the outflow velocity v_{out} as the LSR velocity of the emission minus the cloud LSR velocity which is 5.3 km s^{-1} (van Kempen et al. 2009).

3. RESULTS

3.1. Continuum

Figure 2 shows the continuum emission from the 12 m array and 7 m array data with only the two 2 GHz wide spectral windows. With the much higher sensitivity provided by the large bandwidth and the coverage of short baselines, our Cycle 1 data reveal a fainter extended structure in continuum in addition to the compact component. This extended structure appears to be elongated (about $10'' \times 5''$, i.e., $4400 \text{ au} \times 2200 \text{ au}$) with its major axis perpendicular to the axis of the outflow. This extended emission curves toward the direction of the redshifted outflow. In particular its southern part seems to follow the shape

of the redshifted outflow cavity. On the eastern side, the faintest emission also appears to follow the shape of the blueshifted outflow cavity. Therefore the extended continuum emission is likely tracing a flattened envelope which is shaped by the outflow cavities on both sides.

The peak of the continuum emission is at $8^{\text{h}}25^{\text{m}}43^{\text{s}}.766$, $-51^{\circ}00'35''.70$ (J2000) and has an intensity of $6.4 \text{ mJy beam}^{-1}$ (0.33 K). The position is consistent with the ALMA Cycle 0 observation (Paper I) and previous *HST* observation of HH 47 IRS (Reipurth 2000). The peak intensity is higher than previously observed (0.15 K from Paper I), which is likely caused by the lower beam-dilution produced by the current beam (which is more than a factor of two smaller than that of the Cycle 0 observations). The angular resolution of our continuum observation is still not high enough to resolve the possible different peaks associated with the binary (i.e., the individual circumstellar disks surrounding each of the binary companions) which have a separation of $0''.26$ (Reipurth 2000). The compact component seen here probably traces a circumbinary envelope. Integrated over a circle with a radius of $8''$, the total flux density of the continuum emission is $11 \pm 0.012 \text{ mJy}$. Such a total flux corresponds to a mass of $0.3 M_{\odot}$, using the method described in Paper I and assuming a dust temperature of 30 K , a gas-to-dust mass ratio of 100, and an emissivity spectral index (β) of 1. The

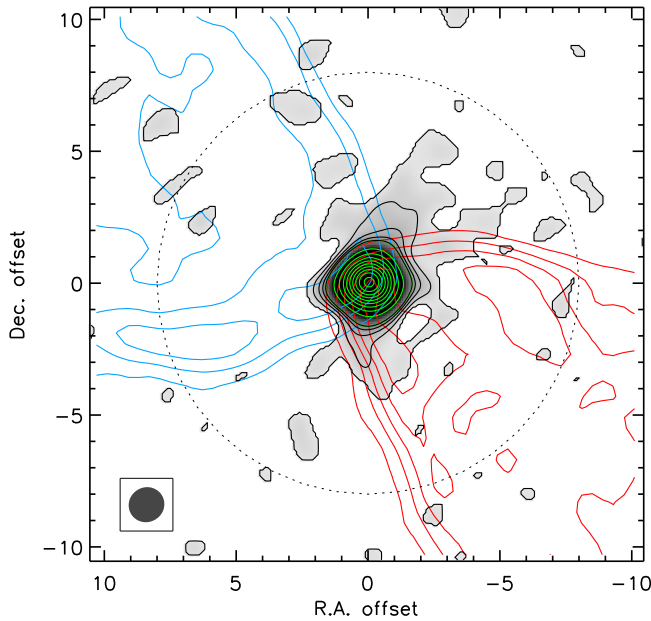


Figure 2. 100 GHz continuum map toward the central source. Only the interferometric data of the two 2 GHz bands are used. Black contours start at 3σ and end at 15σ with a step of 3σ . Here $1\sigma = 0.041 \text{ mJy beam}^{-1}$ (2.32 mK). Green contours start at 30σ with a step of 15σ to show the high intensity part. The highest contour level is 150σ . The synthesized beam of the continuum map is $1.^{\prime\prime}48 \times 1.^{\prime\prime}41$ with P.A. = -77.3° . The red and blue contours show redshifted and blueshifted ^{12}CO outflows for reference. The dashed circle defines the region we integrate to obtain the total flux.

dust opacity (κ) at 3 mm is estimated to be $0.9 \text{ cm}^2 \text{ g}^{-1}$, by extrapolating the value of κ at 1.3 mm obtained by Ossenkopf & Henning (1994) for dust with a thin ice mantle after 10^5 years of coagulation at a gas density of 10^6 cm^{-3} .

3.2. ^{12}CO (1–0)

The integrated emission of the ^{12}CO (1–0) line is shown in Figure 3. Compared with the Cycle 0 observation, the resolution is improved by a factor of 2.4, and the extended emission is recovered. The integrated map in the velocity range from -0.6 to 0.6 km s^{-1} relative to the cloud velocity shows mainly the emission from the host globule with its edges highlighted. The molecular outflow lobes stop at the edge of the globule, therefore there is a drastic contrast in the sizes of the blueshifted and the redshifted lobes. The blueshifted lobe is short with most of its emission concentrated on the outflow cavity wall with a parabolic shape. In contrast, being more deeply embedded, the redshifted outflow contains a large amount of gas inside of the outflow cavity. Three bright clumps are seen inside the red lobe along the outflow axis, at distances of approximately $40''$, $80''$, and $110''$ from the central source (identified as R1, R2, and R3 in Paper I). More extended emission is also detected connecting these clumps to the outflow cavity walls, following the shapes of bow shocks with the apices at the three clumps. This is consistent with a scenario in which these structures trace material entrained by a series of bow shocks caused by episodic ejection events in the jet. The blueshifted outflow also shows a structure that appears at very low velocities (shown in gray scale), tracing the northern cavity wall and a jet-like component (approximately along the outflow axis) connecting the base and the end of the outflow lobe. It is

unclear if the latter structure traces material entrained by the blueshifted jet seen at optical wavelengths.

Figure 4 shows the channel maps of the ^{12}CO (1–0) emission, with a channel width of 0.3 km s^{-1} for the velocity range from -3.6 to 3.6 km s^{-1} relative to the cloud velocity and a channel width of 5 km s^{-1} for higher velocities. We detect emission up to about -30 km s^{-1} for the blueshifted outflow and about 35 km s^{-1} for the redshifted outflow with the 5 km s^{-1} channel width. The blueshifted outflow is seen at velocities $\lesssim -0.9 \text{ km s}^{-1}$. At velocities $\gtrsim -3 \text{ km s}^{-1}$, the blueshifted outflow follows a parabolic shape outlining the outflow cavity, except there is a feature toward the southwest separated from the main outflow. The latter is argued in Paper I to be a second outflow possibly driven by the binary companion of the protostar driving the main outflow. However, we are still not able to identify its counter-lobe. At a higher velocity (e.g., $\lesssim -8 \text{ km s}^{-1}$), the emission forms elliptical rings and moves further away from the central source. This feature can be explained as outflowing shells entrained by a wide-angle wind and will be discussed in detail in Section 4.2.

The redshifted outflow cavity structure is seen at velocities $\gtrsim 1.2 \text{ km s}^{-1}$. As the velocity increases, the outflow cavity becomes narrower, which is most evident at the base of the outflow close to the central source. The northern cavity wall of the redshifted outflow shows at least two parallel thin structures at velocities between 1.8 and 3.6 km s^{-1} (marked by red arrows in Figure 4). Such structures were noticed in the Cycle 0 data (Paper I). With the new higher resolution data, we see that these layers start at only about $40''$ from the central source and extend to about $90''$ from the central source (i.e., nearly 0.13 pc on the plane of the sky). The inner layer curves toward the R2 clump on the jet axis (see the channel map at 2.4 km s^{-1}), while the outer layer extends further and curves toward clump R3 (e.g., the channel map at 3.6 km s^{-1}). We believe these structures trace the material in shells formed in multiple jet bow-shock events and we will discuss them further in Section 4.2.

At velocities from -0.6 to 0.6 km s^{-1} , most of the emission is associated with the parent cloud. However, at the velocity of 0.6 km s^{-1} , bright emission is seen toward the northeast of the central source, which overlaps with the HH 46 reflection nebula and the blueshifted outflow and likely corresponds to the emission from the back side of the northeast (mostly blueshifted) lobe.

3.3. ^{13}CO (1–0)

We show the channel maps of the ^{13}CO (1–0) emission in Figure 5, with a channel width of 0.1 km s^{-1} for velocities within 1.2 km s^{-1} relative to the cloud velocity and a channel width of 0.5 km s^{-1} for higher velocities. ^{13}CO is a higher column density tracer than ^{12}CO , which allows it to trace medium density (about 10^3 cm^{-3}) material in a globule (e.g., Arce & Sargent 2005). Here it is only detected at relatively low outflow velocities from -2.5 to 3.5 km s^{-1} . The blueshifted outflow is seen at velocities from -2.5 to -0.8 km s^{-1} . At velocities from -2.5 to -1.5 km s^{-1} the ^{13}CO traces a V-shaped outflow cavity, but with no emission inside the apparent cavity structure unlike ^{12}CO at these velocities. In addition the emission is brighter in the southern cavity wall as opposed to what is seen in ^{12}CO . The second outflow toward the southeast of the central source is seen at velocities from -1.5 to -0.8 km s^{-1} . The emission at velocities from -0.6 to 0.2 km s^{-1} is dominated by the cloud material, which shows

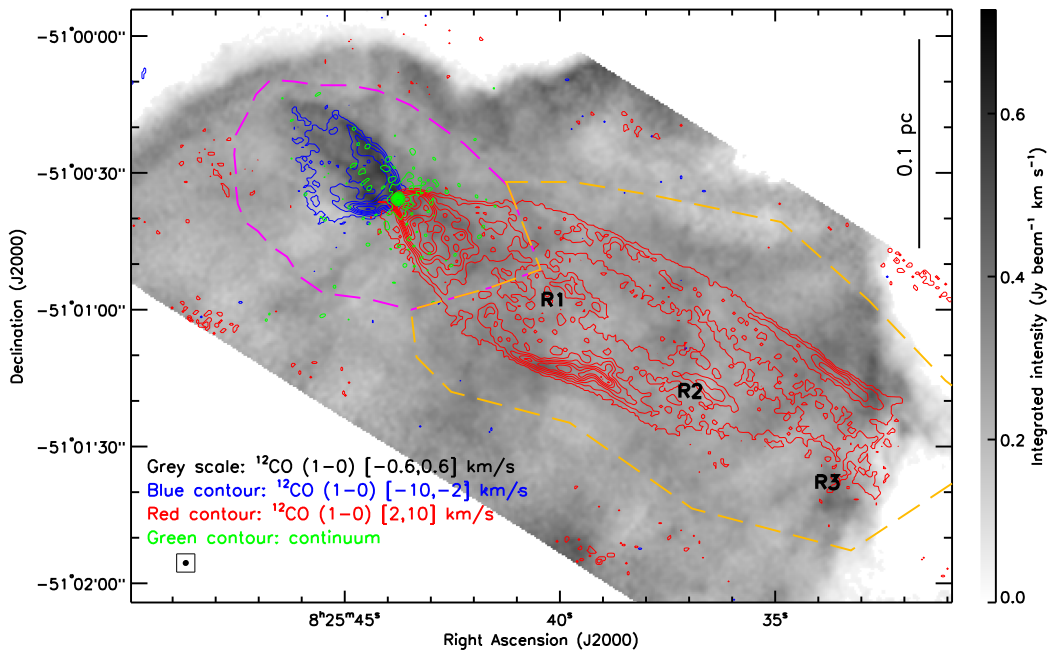


Figure 3. Integrated intensity maps of the HH 46/47 ^{12}CO (1–0) emission. The blue contours represent the blueshifted emission integrated from -10 to -2 km s^{-1} relative to the cloud velocity. The red contours represent the redshifted emission integrated from 2 to 10 km s^{-1} . The blue and red contours start at 3σ and have a step of 6σ ($\sigma = 0.023 \text{ Jy beam}^{-1} \text{ km s}^{-1}$). The gray scale represents the ^{12}CO (1–0) emission integrated over velocity range from -0.6 to 0.6 km s^{-1} relative to the cloud velocity. The synthesized beam of ^{12}CO is $1.^{\prime\prime}37 \times 1.^{\prime\prime}31$ (P.A. = $-58.^{\circ}2$). The green contours show the 100 GHz continuum emission. The contours start at 3σ and have a step of 15σ ($\sigma = 0.041 \text{ mJy beam}^{-1}$). The labels R1, R2, R3 mark the positions of the three bright clumps on the outflow axis (see Sections 3.2 and 4.2 for more details). The dashed lines define two sub-regions: the central region (purple lines) covering the blueshifted outflow and the base of the redshifted outflow, and the extended red lobe (yellow lines) covering the rest of the redshifted outflow. The morphology of ^{13}CO and C^{18}O emission has been taken into account when defining these regions. These regions are used in Section 3.7 in order to exclude emission that is not associated with the outflow.

clumpy structures toward the south and southwest of the central source. The redshifted outflow cavity, especially the northern cavity wall, appears at a velocity as low as 0.2 km s^{-1} . At velocities higher than 0.8 km s^{-1} the ^{13}CO emission mainly traces the limb-brightened outflow cavity. The cavity forms a loop with its end coincident with the ^{12}CO clump R2. In the vicinity of the central source, the peak of the ^{13}CO emission moves from north of the source at velocities between approximately -0.6 and 0 km s^{-1} to south of the source at velocities between 0 and 0.6 km s^{-1} . The velocity gradient is perpendicular to the direction of the outflow and suggests a rotating envelope, consistent with the gradient observed in C^{18}O (see below).

3.4. C^{18}O (1–0)

We show the channel maps of the C^{18}O (1–0) emission in Figure 6. Being a higher column density tracer than ^{13}CO , C^{18}O typically traces gas with densities approximately 10^4 to 10^5 cm^{-3} inside molecular clouds (e.g., Fuller & Ladd 2002). With a channel width of 0.1 km s^{-1} , the emission is only detected within 1 km s^{-1} from the cloud velocity. At blueshifted velocities, the emission traces the clumpy structures inside the parent globule extending from the central source to the south and southwest, which also appear in the ^{13}CO (1–0) emission at these velocities. The blueshifted outflow cavity is not detected in this line. The northern cavity wall of the redshifted outflow starts to appear at a velocity as low as 0.2 km s^{-1} and dominates the morphology of the C^{18}O emission up to 0.8 km s^{-1} . The southern cavity wall of the redshifted outflow appears at velocities from 0.4 to 0.8 km s^{-1} but only at regions close to the central source. The limb-brightened

outflow cavity in C^{18}O may arise from material accelerated by the outflow piled up along the cavity walls or from a higher excitation temperature or a higher abundance due to the interaction of the outflow and the core. Only the red lobe is detected in this high column density tracer because it is more embedded in the cloud than the blue lobe. In the vicinity of the central source, the emission peak moves from the north of the source at blueshifted velocities (from -0.6 to 0 km s^{-1}) to the south of the source at redshifted velocities (from 0 to 0.6 km s^{-1}), which could be interpreted as rotation (see Section 4.3).

3.5. CS (2–1)

In Figure 7 we show the channel maps of the CS (2–1) emission. CS is typically a tracer of material at densities greater than approximately 10^4 cm^{-3} (Mardones et al. 1997). Between about -0.8 and 0.2 km s^{-1} , most of the emission traces the cloud structures toward the south and southwest of the central source, which also appear in ^{13}CO and C^{18}O . The blueshifted outflow cavity is not detected, while the redshifted outflow cavity appears at velocities from about 0.2 to 1 km s^{-1} . Especially around 0.6 – 0.8 km s^{-1} the emission forms a loop outlining the redshifted outflow cavity with its end coinciding with the ^{12}CO clump R2. Above 1 km s^{-1} the CS emission mainly traces a collimated structure inside the outflow cavity. The region where the southern outflow cavity wall ends is also visible in CS at these velocities. The jet-like structure in CS overlaps with the ^{12}CO emission inside the outflow cavity along the length of the infrared jet (as seen in the maps presented by Noriega-Crespo et al. 2004 and Velusamy et al. 2007), suggesting that the CS also probes the jet-

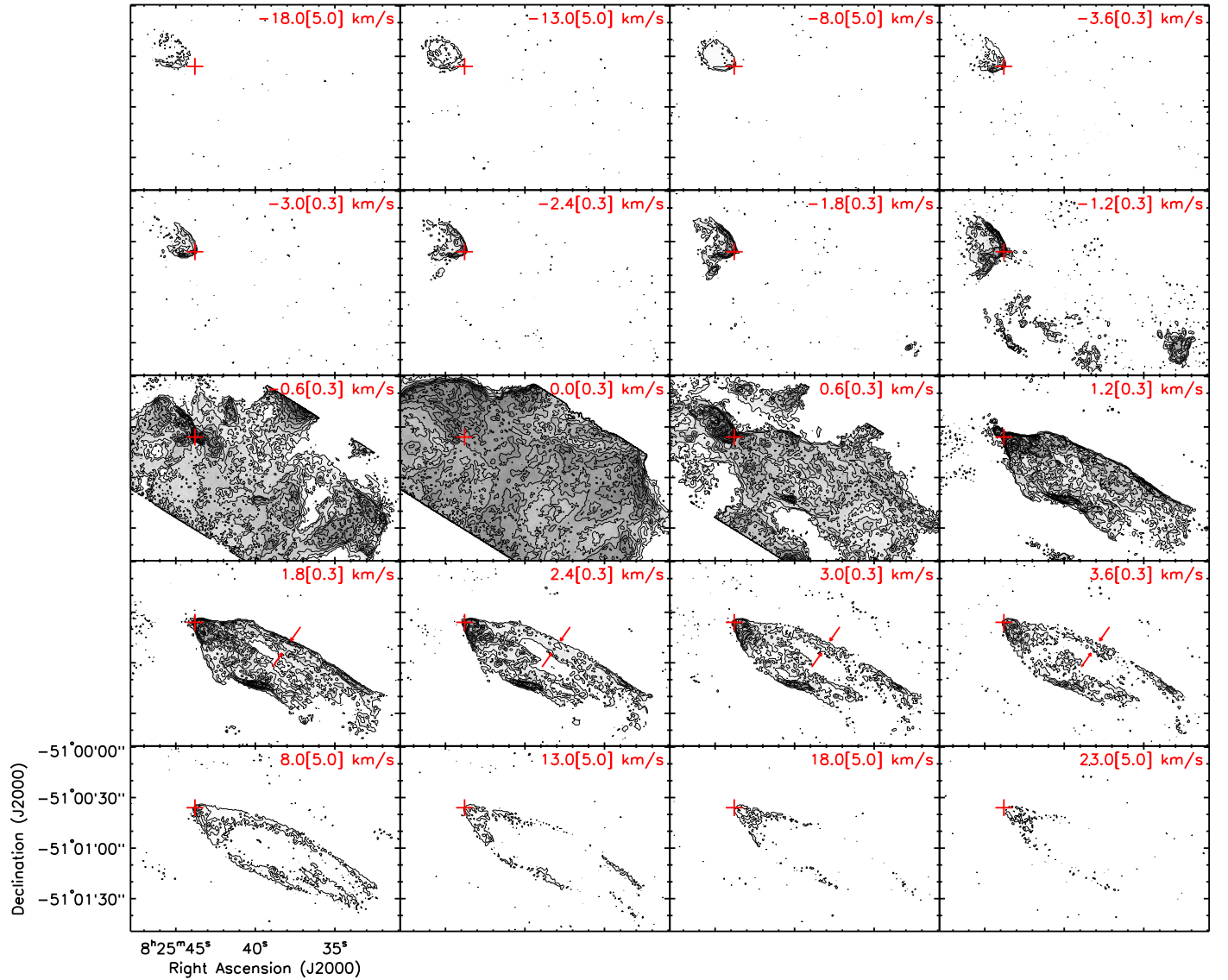


Figure 4. Channel maps of the ^{12}CO (1–0) emission. In the upper right corner of each panel, the central outflow velocity relative to the cloud velocity and the width of the channel (in parenthesis) are given. The contours start at 3σ with a step of 6σ . $1\sigma = 3.4 \text{ mJy beam}^{-1}$ for channels with a width of 5 km s^{-1} , and 11 mJy beam^{-1} for channels with a width of 0.3 km s^{-1} . The synthesized beam is $1''.37 \times 1''.31$ (P.A. = $-58^\circ 2$). The red crosses mark the position of the peak of the continuum emission. The red arrows in the panels on the fourth row mark where the thin structures on the outflow cavity wall bifurcate (see Sections 3.2 and 4.2 for more details).

entrained material inside the outflow cavity. The kinematics of this structure will be discussed in Section 4.4.

3.6. C^{17}O (1–0) and C^{34}S (2–1)

The C^{17}O (1–0) emission of the HH 46/47 outflow is only detected in the 7 m array and total power data, which is shown in the upper panel of Figure 8. We detect the three hyperfine lines of C^{17}O (1–0), with a width of about 0.5 km s^{-1} for each of them. Toward the central source there is bright C^{17}O emission with its peak slightly to the northwest of the central source, tracing the immediate envelope. Extending to the west, C^{17}O appears to follow the shape of the redshifted ^{12}CO outflow, with little emission inside of the cavity, clearly suggesting that the outflow has created a low column density cavity from the parent globule. There is a distinct C^{17}O clump close to the bright ^{12}CO emission on the southern wall of the red lobe, which we believe is a dense clump that the outflow is

interacting with and produces the kink in the ^{12}CO cavity wall. The high column density material also extends further to the south of the central source, similar to the ^{13}CO and C^{18}O maps.

The C^{34}S (2–1) emission is also only detected in the 7 m array and total power data within the velocity range from -0.6 to 0.6 km s^{-1} , which is shown in the lower panel of Figure 8. The C^{34}S appears to trace a linear structure inside the globule starting from where the central source is and extending to the south. The cavity carved out by the redshifted outflow is also seen.

3.7. Mass, Momentum, and Kinetic Energy of the Outflow

To accurately estimate the mass, momentum, and energy of the CO outflow requires properly correcting for the optical depth of the lines used for estimating the column densities. The fact that most of the outflowing material is at low velocities and that ^{12}CO is optically thick at these velocities leads to a severe

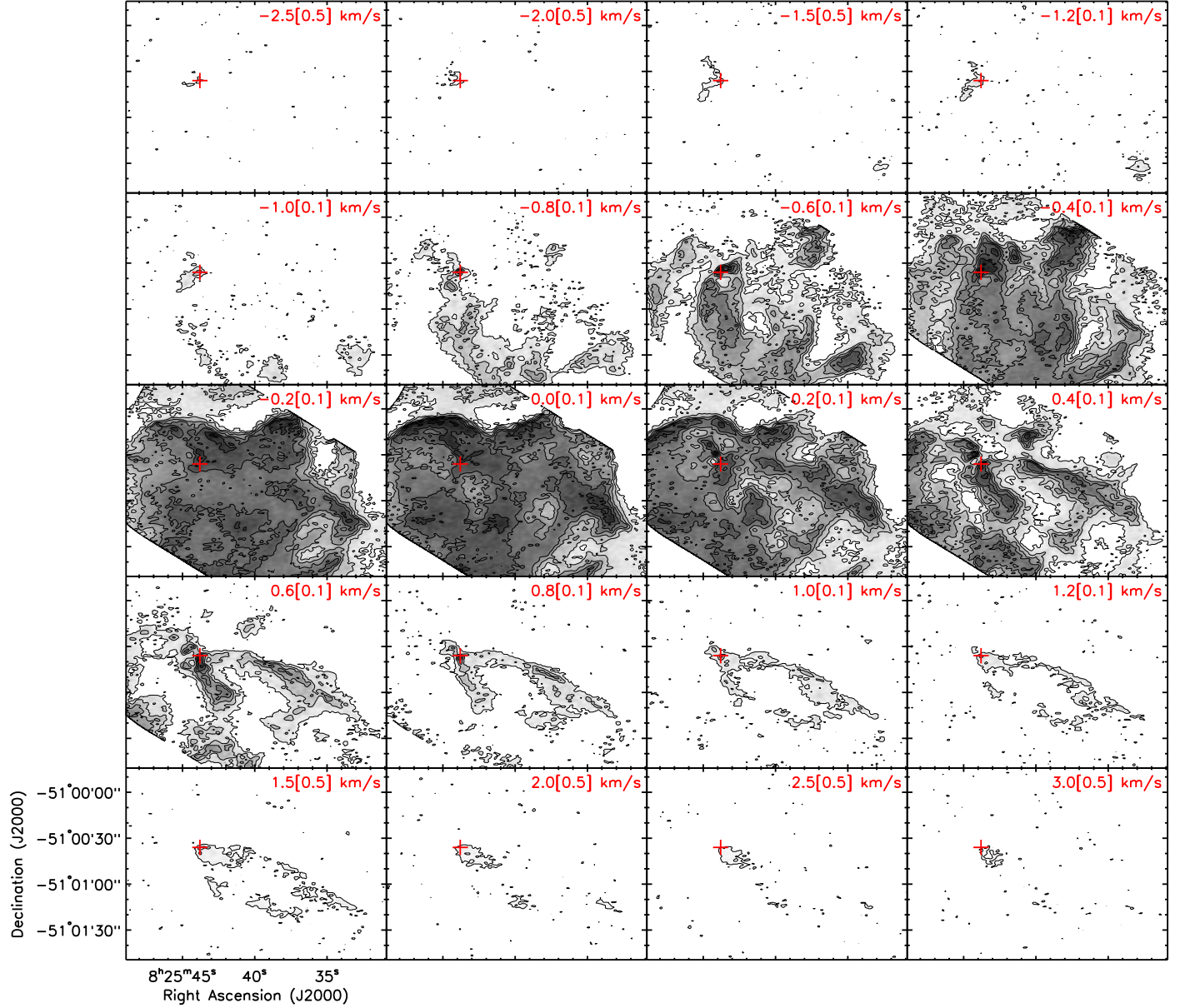


Figure 5. Channel maps of the ^{13}CO (1–0) emission. In the upper right corner of each panel, the central outflow velocity relative to the cloud velocity and the width of the channel (in parentheses) are given. The contours start at 3σ with a step of 9σ . $1\sigma = 7.4 \text{ mJy beam}^{-1}$ for channels with a width of 0.5 km s^{-1} and 13 mJy beam^{-1} for channels with a width of 0.1 km s^{-1} . The synthesized beam is $3.^{\prime\prime}18 \times 1.^{\prime\prime}67$ (P.A. = $-86^{\circ}1$). The red crosses mark the position of the peak of the continuum emission.

underestimate of the mass if simply assuming it is optically thin (e.g., Arce & Goodman 2001b; Dunham et al. 2014). One way to estimate the optical depth of ^{12}CO is to use the intensity ratio between ^{12}CO and one of its optically thinner isotopologues (usually ^{13}CO). However, ^{13}CO itself maybe optically thick at low velocities ($\lesssim 1 \text{ km s}^{-1}$). Here, with observations of ^{12}CO , ^{13}CO , and C^{18}O with similar sensitivities and angular resolutions we are able to estimate the ^{12}CO and ^{13}CO optical depths and therefore much more accurately measure the outflow properties.

We estimate the correction factor to the optical depth following the method outlined by Dunham et al. (2014) but applied to three CO isotopologues ^{12}CO , ^{13}CO and C^{18}O . A detailed formulation can be found in the Appendix. Assuming ^{12}CO , ^{13}CO , and C^{18}O approximately trace the same material

and have the same excitation temperature T_{ex} and beam filling factor, and that C^{18}O is optically thin, we have

$$\begin{aligned} \frac{T_{R,13}(v)}{T_{R,18}(v)} &= \frac{1 - \exp(-\tau_{v,13})}{1 - \exp(-\tau_{v,18})} \\ &= \frac{1 - \exp(-\tau_{v,13})}{\tau_{v,18}} \\ &\approx X_{13,18} \frac{1 - \exp(-\tau_{v,13})}{\tau_{v,13}}, \end{aligned} \quad (1)$$

where the subscripts 13 and 18 represent ^{13}CO and C^{18}O , respectively, and $X_{13,18}$ is the abundance ratio between ^{13}CO and C^{18}O . To correct for the optical depth of ^{13}CO , we simply

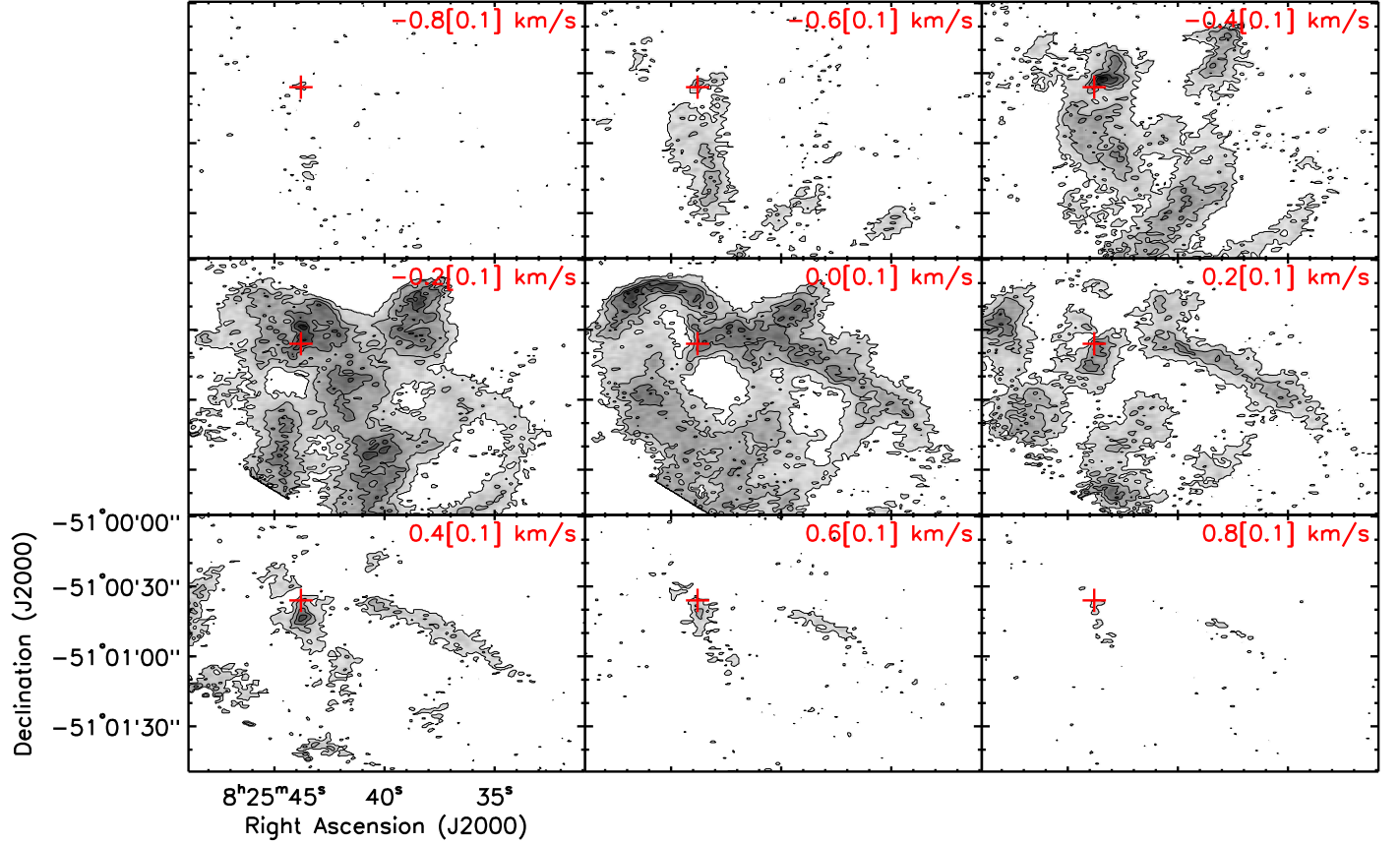


Figure 6. Channel maps of the C¹⁸O (1–0) emission. The central outflow velocity relative to the cloud velocity and the width of the channel are shown in the upper right corner of each panel. The contours start at 3σ with a step of 6σ ($1\sigma = 13 \text{ mJy beam}^{-1}$). The synthesized beam is $3''20 \times 1''.69$ (P.A. = -86°). The red cross shows the peak of the continuum emission.

need to multiply the measured ¹³CO intensity by a factor

$$F_{\tau,13}(v) \equiv \frac{\tau_{v,13}}{1 - \exp(-\tau_{v,13})} = X_{13,18} \frac{T_{R,18}(v)}{T_{R,13}(v)}. \quad (2)$$

Similarly, the optical depth correction factor for ¹²CO is

$$F_{\tau,12}(v) = X_{12,13} \frac{T'_{R,13}(v)}{T_{R,12}(v)}, \quad (3)$$

where $T'_R \equiv T_R(v)F_\tau$ is the optical-depth-corrected intensity. Note, the intensity ratio has an upper limit equal to the abundance ratio, therefore the correction factors have a lower limit of 1. In this paper, we adopt $X_{12,13} = 62$ (Langer & Penzias 1993), $X_{13,18} = 8.7$ (from $[^{16}\text{O}]/[^{18}\text{O}] = 540$, Wilson & Matteucci 1992).

Figure 9 shows the mean intensity ratios between ¹³CO (1–0) and C¹⁸O (1–0) as a function of velocity. In each velocity channel, we first calculate the intensity ratios between the two lines at the pixels where both lines are detected above 5σ . Only the pixels within the defined sub-regions shown in Figure 3 are included since in this work we only focus on the outflow. The uncertainties of these pixel intensity ratios are calculated from the channel map rms errors using error propagation. We then calculate the weighted mean and weighted standard deviation of these pixel intensity ratios in each channel (data points and error bars in the figure). The weights are inversely proportional to the square of the uncertainties of the pixel intensity ratios. In such a way, the pixels with both lines detected with higher

signal-to-noise ratio carry more weight. In order to estimate the optical depth of ¹³CO at higher velocities where the C¹⁸O line is not detected, we fit a parabola to the measured intensity ratios with the minimum point fixed at zero velocity (Arce & Goodman 2001b; Offner et al. 2011; Dunham et al. 2014). Note that the intensity ratio reaches its upper limit, the abundance ratio between the two molecules, at velocities where both transitions are optically thin. The fitted parabola (solid curve) is

$$T_{13}/T_{18} = (2.91 \pm 0.40) + (5.46 \pm 1.48)(v - v_{\text{rest}})^2 \quad (4)$$

with a reduced χ^2 of 0.22. According to this, the ¹³CO (1–0) line becomes optically thin at velocities higher than 1 km s^{-1} .

Figure 10 shows the mean intensity ratios between ¹²CO (1–0) and ¹³CO (1–0) as a function of velocity. The ratios are calculated in the same way as the ¹³CO-to-C¹⁸O intensity ratios. Again only the emission within the outflow region is included in the calculation. Without correcting the optical depth of ¹³CO, the intensity ratios become flat at low velocities (blue symbols), suggesting optically thick ¹³CO emission. After correcting for the ¹³CO optical depth, we can fit a parabola even at the low velocities. The best fit for the region of the whole outflow is

$$T_{12}/T'_{13} = (0.47 \pm 0.053) + (3.46 \pm 0.14)(v - v_{\text{rest}})^2 \quad (5)$$

and the reduced χ^2 is 0.82. From this fit, ¹²CO (1–0) becomes optically thin at velocities higher than 4.2 km s^{-1} .

To calculate the mass of the molecular outflow requires an estimate of the CO excitation temperature (T_{ex}). There are various estimates of T_{ex} for this outflow in the literature. Chernin &

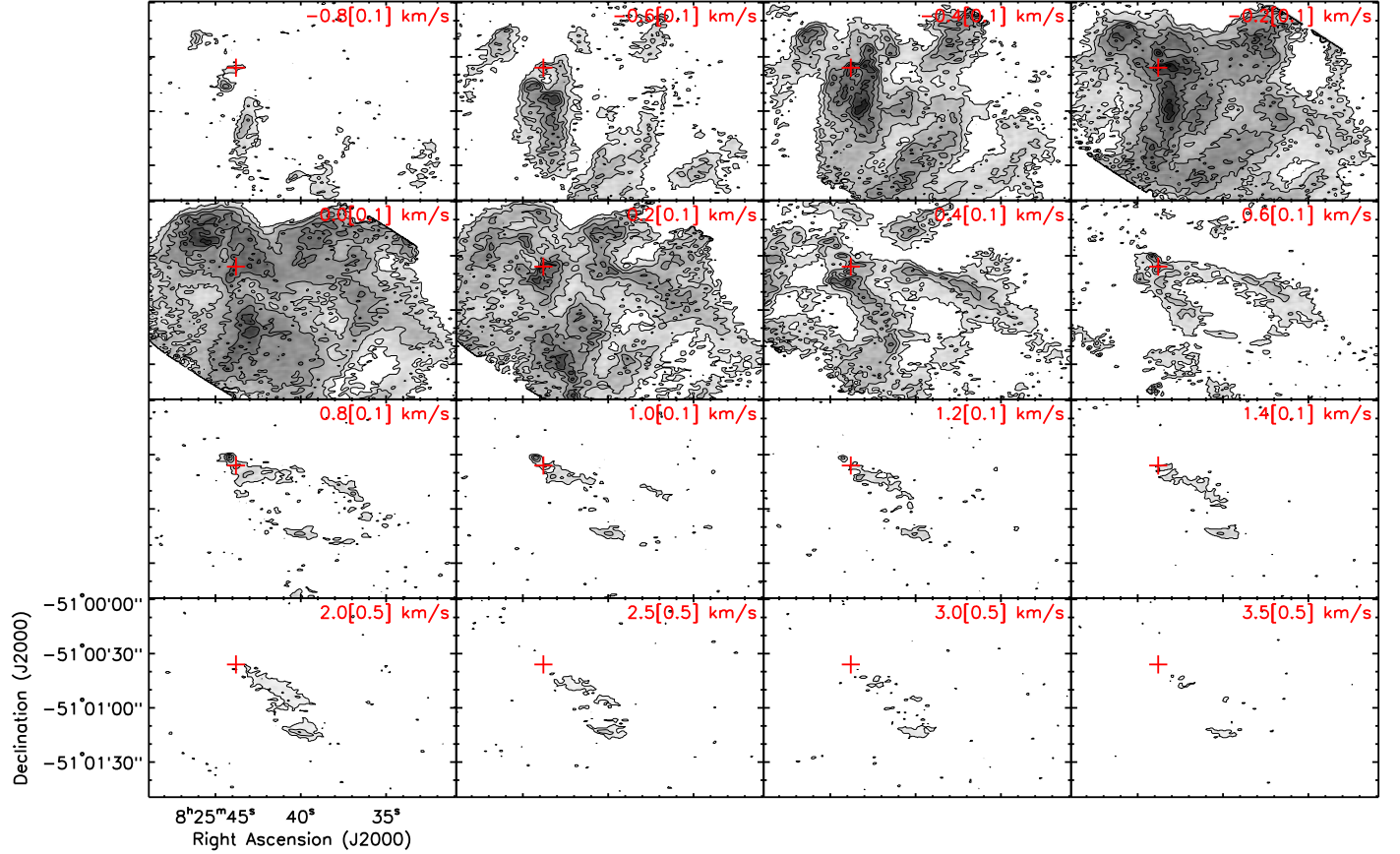


Figure 7. Channel maps of the CS (2–1) emission. The central outflow velocity relative to the cloud velocity and the width of the channel are shown in the upper right corner of each panel. The contours start at 3σ with a step of 6σ . $1\sigma = 10 \text{ mJy beam}^{-1}$ for channels with a width of 0.1 km s^{-1} , and $5.5 \text{ mJy beam}^{-1}$ for channels with a width of 0.5 km s^{-1} . The synthesized beam is $3.^{\prime\prime}62 \times 1.^{\prime\prime}92$ (P.A. = $-86^{\circ}6$). The red cross show the peak of continuum emission.

Masson (1991) estimated an outflow excitation temperature of $8.4 \pm 1 \text{ K}$ using the ^{12}CO (3–2) and ^{12}CO (2–1) brightness temperature ratio. Olberg et al. (1992) estimated an excitation temperature of 15 K at outflow velocities using the intensity ratio between ^{12}CO (1–0) and ^{12}CO (2–1). van Kempen et al. (2009) estimated an excitation temperature of about 100 K along the redshifted outflow axis and about 60 K for the blueshifted outflow, using low- and high- J transitions of CO. We also can estimate the excitation temperature from the measured optically thick brightness temperature of ^{12}CO at low velocities. Within 4 km s^{-1} relative to the cloud velocity where the ^{12}CO (1–0) is optically thick, from Equation (11) we can estimate the excitation temperature to be $T_{\text{ex}} = 5.53/\ln[1 + 5.53/(T_R + 0.82)]$ (assuming a beam filling factor of 1). At these velocities, the peak intensities of the ^{12}CO (1–0) line range from about 13 to 45 K, i.e., $T_{\text{ex}} = 16\text{--}49 \text{ K}$, consistent with the excitation temperature from previous observations and appropriate for the gas traced by the CO (1–0) line. In the rest of the paper, we will calculate the mass and other properties of the outflow using two typical values of T_{ex} , 15 and 50 K.

To calculate the mass and other properties of the outflow also requires separating the outflow material from the cloud material. At low velocities, e.g., less than 1 km s^{-1} relative to the cloud velocity, the outflow cavity structure is already apparent, but there is also considerable emission from cloud material (not associated with the outflow). One way to disentangle these two components is to fit the low-velocity part of the mass spectrum with a Gaussian distribution and subtract such a component from the total emission (e.g., Arce

& Goodman 2001b; Dunham et al. 2014). However, instead of just a total value, we are interested in the spatial distribution of the outflow material. Therefore we simply apply a velocity boundary to exclude the contribution of the cloud material. For ^{12}CO , we only include the emission with $|v_{\text{out}}| \geq 0.9 \text{ km s}^{-1}$ in the central region and $v_{\text{out}} \geq 0.9 \text{ km s}^{-1}$ or $v_{\text{out}} \leq -1.2 \text{ km s}^{-1}$ in the extended red lobe. For ^{13}CO , we only include the emission with $v_{\text{out}} \leq -0.8 \text{ km s}^{-1}$ or $v_{\text{out}} \geq 0.4 \text{ km s}^{-1}$ in the central region and $v_{\text{out}} \leq -0.9 \text{ km s}^{-1}$ or $v_{\text{out}} \geq 0.4 \text{ km s}^{-1}$ in the extended red lobe. For C^{18}O , we only include the emission with $v_{\text{out}} \geq 0.2 \text{ km s}^{-1}$ in the extended red lobe. We then calculate the column density of ^{12}CO , ^{13}CO , and C^{18}O (after correcting for the optical depth) at each velocity channel, using Equation (15) assuming local thermodynamic equilibrium (LTE) conditions and a beam filling factor of 1. We adopt an abundance of ^{12}CO of 10^{-4} relative to H₂ and a gas mass of $2.34 \times 10^{-24} \text{ g per H}_2 \text{ molecule}$. Combining the column densities calculated from the three CO isotopologues in different pixels and velocity channels, we obtain a combined column density map. At the pixels where more than one CO isotopologue is detected, we choose the highest column density calculated from these CO isotopologues.

In Figure 11 we show the spatial distributions of the mass, momentum, and kinetic energy of the outflow, combining the three CO isotopologues and using $T_{\text{ex}} = 15 \text{ K}$ as an example. The momentum surface density is defined as $P_{\text{out}} = \sum_{v_{\text{out}}} M(x, y, v_{\text{out}}) v_{\text{out}}$ and the energy surface density

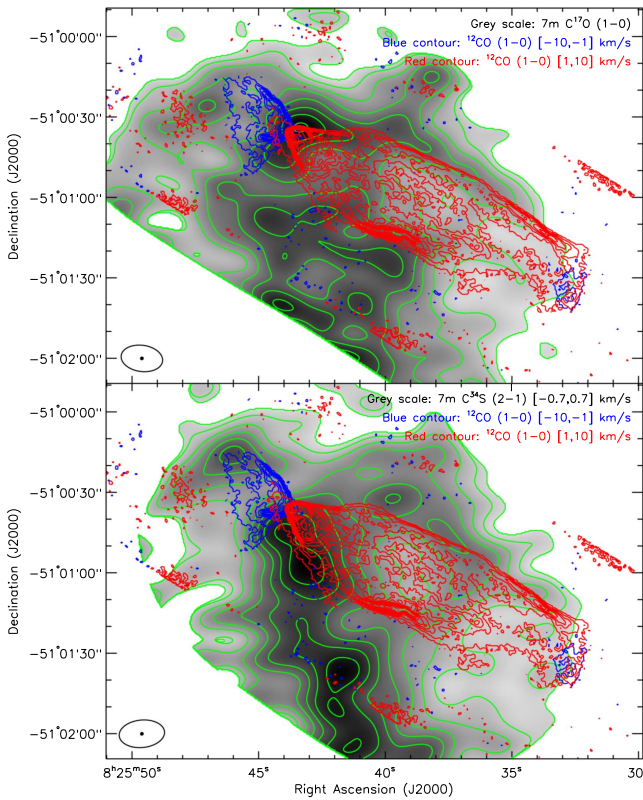


Figure 8. Upper panel: the integrated emission of the $C^{17}O$ (1–0) line combining the 7 m array and total power data in gray scale and green contours, overlaid with the blue contours and red contours showing the ^{12}CO (1–0) emission integrated in the velocity range from -10 to -1 km s^{-1} and from 1 to 10 km s^{-1} . The $C^{17}O$ (1–0) emission is integrated over 5 km s^{-1} to cover the three hyperfine lines spanning 1.2 MHz (about 4 km s^{-1}). The green contours start at 3σ and have a step of 3σ ($1\sigma = 0.043 \text{ Jy beam}^{-1} \text{ km s}^{-1}$). The blue and red contours start at 3σ and have a step of 6σ ($1\sigma = 0.023 \text{ Jy beam}^{-1} \text{ km s}^{-1}$). The synthesized beam of $C^{17}O$ is $15.''6 \times 9.''8$ (P.A. = -82.1°). Lower panel: same as the upper panel but showing the $C^{34}S$ (2–1) emission combining the 7 m array and the total power data integrated from -0.7 to 0.7 km s^{-1} in gray scale and green contours. The green contours start at 3σ and have a step of 3σ ($1\sigma = 0.016 \text{ Jy beam}^{-1} \text{ km s}^{-1}$). The synthesized beam of $C^{34}S$ is $17.''0 \times 10.''3$ (P.A. = -84.6°).

$E_{\text{out}} = \sum_{v_{\text{out}}} M(x, y, v_{\text{out}}) v_{\text{out}}^2 / 2$, where $M(x, y, v_{\text{out}})$ is the mass surface density of the outflow in each velocity channel, and v_{out} is not corrected for inclination. Therefore they only provide lower limits for the real momentum and energy distributions. Compared with the mass map, the momentum and energy are more concentrated toward the outflow cavity walls around the central source, as they are more dominated by the high-velocity material. In the kinetic energy distribution map (lower panel of Figure 11), we see highlighted outflow cavity walls and even jet-like structures at the base of the outflow on both sides. The southern wall of the blue lobe is more prominent than the northern wall in the energy map, in contrast to the mass map. The three shocked regions inside the red lobe (R1, R2, and R3) are clearly seen in the energy map, however, most of the energy is not around these clumps, which mark the apices of a series of jet bow shocks, as it is predicted by jet entrainment models. Rather, most of the energy is along the cavity walls at the base of the outflow. This suggests that even though the jet bow-shock features dominate the morphology of the red lobe (see discussions in Section 4.2), the contribution of a wide-angle wind may dominate the energy input. This is also supported by

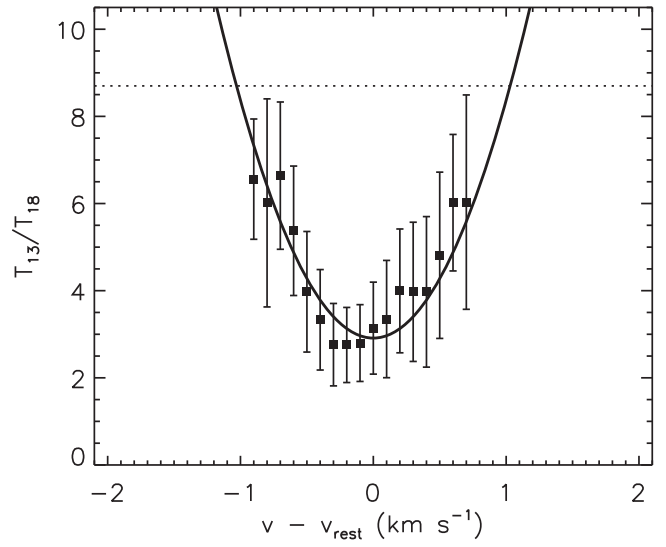


Figure 9. Intensity ratio between ^{13}CO (1–0) and $C^{18}O$ (1–0) as a function of velocity. At each velocity, the data point and the error bar are the weighted mean and weighted standard deviation of the intensity ratios over the pixels where both ^{13}CO (1–0) and $C^{18}O$ (1–0) are detected above 5σ (see text). Only the pixels within the two defined sub-regions (see Figure 3) are included. The solid curve is the best-fit second-order polynomial, and the dotted lines indicate the abundance ratio which sets the upper limit of the intensity ratio.

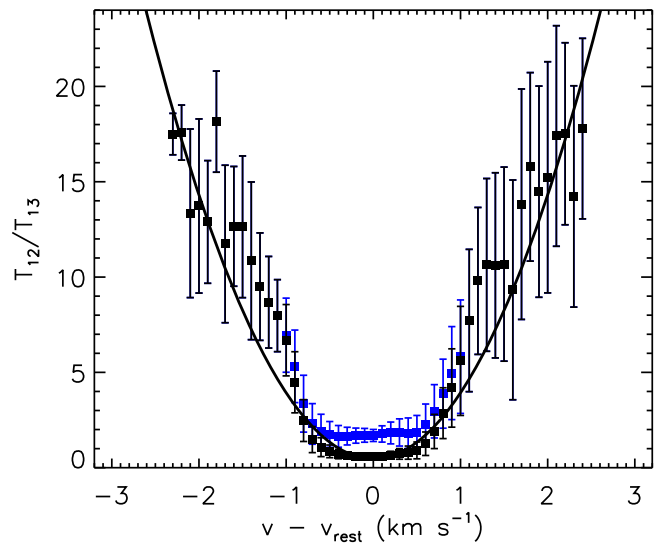


Figure 10. Same as Figure 9, but showing the intensity ratios between ^{12}CO (1–0) and the optical-depth-corrected ^{13}CO (1–0) emission (black symbols, error bars). The blue symbols and error bars are the ratios and uncertainties using the original ^{13}CO intensities. The solid curve is the best-fit second-order polynomial using the black data points.

the fact that the blueshifted and the redshifted outflows appear to be more symmetric in the energy map (the brightest part) since the high-velocity component of the blueshifted outflow is mainly entrained by a wide-angle wind (see Section 4.2).

In Figure 12 we show the velocity distribution of the outflow mass, assuming an excitation temperature of 15 K . The correction for the CO optical depth and including the higher column density tracers significantly increases the estimated mass at velocities $\lesssim 4 \text{ km s}^{-1}$ (by more than an order of magnitude at velocities below 1 km s^{-1}). The slopes of the mass spectra become much steeper after such corrections. We fit the combined mass spectra with power laws in a form of m

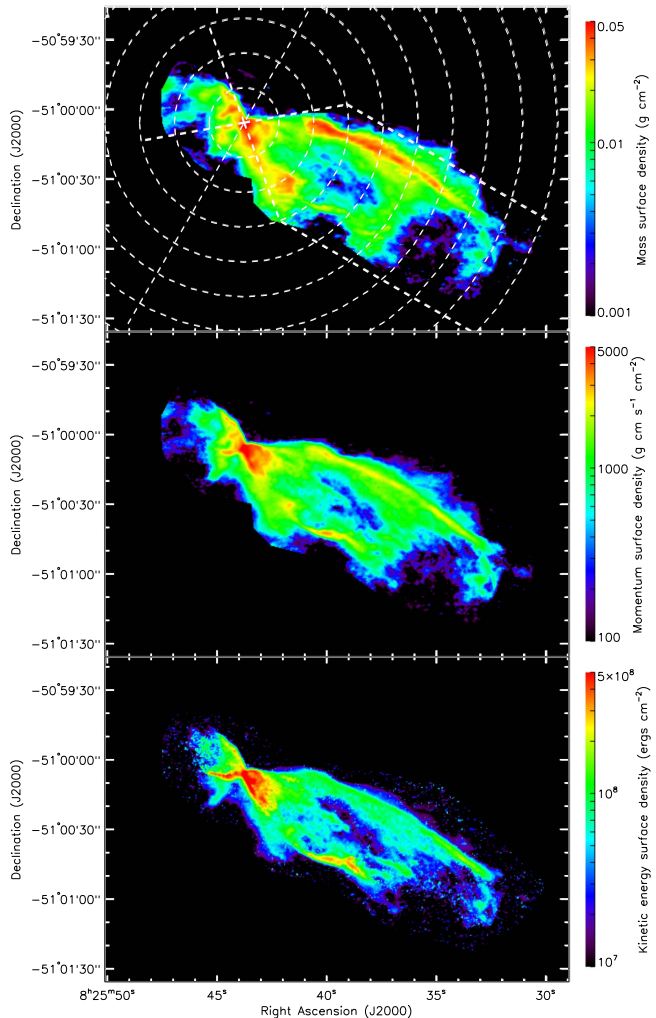


Figure 11. Surface density maps of the mass, momentum, and kinetic energy (from top to bottom) of the HH 46/47 outflow. Only the emission considered to be associated with the outflow has been taken into account. The maps combine the material traced by ^{12}CO , ^{13}CO , and C^{18}O (see text). The dashed circles show the annuli over which we integrate to obtain the mass distribution with respect to the distance from the central source in Figure 13. The dashed diagonal line divides the blue lobe and the red lobe. The other dashed lines roughly outline the outflow cavities which are used to estimate the mass of the ambient material which originally filled the outflow cavity (see Figure 13 and Section 4.1).

$(v) \propto v^{-\gamma}$ in the velocity range of $0.6 \leq |v_{\text{out}}| \leq 15 \text{ km s}^{-1}$ for the redshifted outflow and $0.9 \leq |v_{\text{out}}| \leq 15 \text{ km s}^{-1}$ for the blueshifted outflow. At lower velocities, the mass spectrum becomes flatter, which is due to the fact that in these channels the outflow structure can only be clearly identified in C^{18}O and ^{13}CO emission, and the ^{12}CO emission is excluded due to the cloud emission. While taking this low-velocity mass into account when calculating the total mass, we exclude it in fitting the slope of the mass–velocity relation. We found a slope of $\gamma = -3.43 \pm 0.04$ for the redshifted outflow and a slope of $\gamma = -2.78 \pm 0.11$ for the blueshifted outflow. The redshifted outflow is much more massive than the blueshifted outflow, but they have similar masses at velocities higher than 10 km s^{-1} . Smith et al. (1997) suggested that the mass spectrum slope steepens as the outflow evolves since as time goes by the material that once had been accelerated starts to slow down gradually. In such a scenario, an outflow in a denser medium

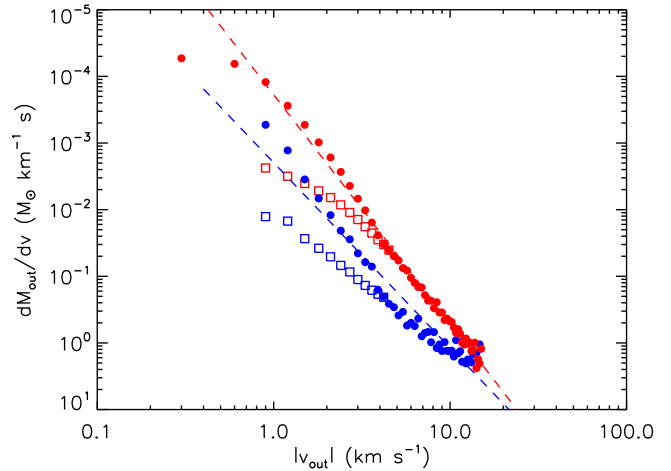


Figure 12. Mass spectra of the HH 46/47 outflow. The blue and red symbols are for the blueshifted and redshifted material, respectively. The open squares show the mass derived from ^{12}CO without optical depth correction. The filled circles show the mass obtained combining the optical-depth-corrected ^{12}CO and ^{13}CO emission, and the C^{18}O data. The dashed lines are power-law fits to the filled circles within the velocity range from 0.6 km s^{-1} (redshifted) or 0.9 km s^{-1} (blueshifted) to 15 km s^{-1} .

will decelerate faster than an outflow in a low density medium (Arce & Goodman 2001b). This may be an explanation for the steeper mass spectrum in the redshifted outflow than the blueshifted outflow in this source. Previous observations also suggested that γ changes at a velocity of about 10 km s^{-1} with a steeper power law for the higher velocity (e.g., Richer et al. 2000). We do not see such two distinct components in this source. Actually, the slope we find here is much steeper than the slopes previously reported for the low-velocity range $v < 10 \text{ km s}^{-1}$ ($-2.5 < \gamma < -1$), but consistent with the slopes reported for the velocity greater than 10 km s^{-1} ($-4 < \gamma < -2.5$), which implies that the previously reported change of slope at about 10 km s^{-1} may be due to uncorrected CO opacity. However, we note that, even with optical depth correction, a few outflows still show a change of slope in the mass spectrum around 10 km s^{-1} (e.g., Su et al. 2004).

Table 1 lists the total masses $M_{\text{out}} = \sum_{x,y,v_{\text{out}}} M(x, y, v_{\text{out}})$, the momentum $P_{\text{out}} = \sum_{x,y,v_{\text{out}}} M(x, y, v_{\text{out}}) v_{\text{out}}$, and the kinetic energy $E_{\text{out}} = \sum_{x,y,v_{\text{out}}} M(x, y, v_{\text{out}}) v_{\text{out}}^2 / 2$ of the redshifted and blueshifted outflows, measured from ^{12}CO , ^{13}CO , and C^{18}O emission and combined, both with and without optical depth corrections. For the momentum and kinetic energy, we also list the values after correcting for the inclination of the outflow with respect to the plane of the sky i , which is assumed to be 40° (see Section 4.2). The correction factor is $1/\sin i$ for P_{out} and $1/\sin^2 i$ for E_{out} . Note that these correction factors are only valid for outflows where all the motion is along the axis. Downes & Cabrit (2007) constructed models of jet-entrained outflow and investigated the effect of inclination correction on momentum and energy estimates, taking into account the transverse motions of the outflow. They found that the correction factor of $1/\sin i$ for P_{out} always overestimates the true momentum while the uncorrected P_{out} actually agrees with the true value. They also found that E_{out} with the $1/\sin^2 i$ correction overestimates the true value, while the value without the inclination correction underestimates the true energy.

Using only ^{12}CO and without correcting for the optical depth, our estimated outflow properties (the values in brackets

Table 1
Mass, Momentum, and Kinetic Energy of the Outflow

Tracer	Lobe ^a	Mass ^b ($10^{-2} M_{\odot}$)		Momentum ^{b,c} ($10^{-2} M_{\odot} \text{ km s}^{-1}$)		Kinetic Energy ^{b,c} (10^{42} erg)	
		$T_{\text{ex}} = 15 \text{ K}$	50 K	15 K	50 K	15 K	50 K
^{12}CO	Blue	8.7 (1.0)	22 (2.4)	11/18 (2.5/3.8)	28/44 (6.1/9.5)	2.4/5.7 (1.2/3.0)	5.8/14 (3.0/7.4)
	Red	49 (5.8)	120 (14)	64/99 (13/20)	157/244 (32/50)	11/28 (4.6/11)	28/68 (11/27)
^{13}CO	Blue	3.5 (3.0)	8.8 (7.6)	3.6/5.6 (3.2/5.0)	9.1/14 (8.1/13)	0.43/1.0 (0.39/0.95)	1.1/2.6 (0.98/2.4)
	Red	98 (52)	244 (129)	53/83 (31/48)	133/207 (78/121)	3.4/8.3 (2.3/5.6)	8.6/21 (5.8/14)
C^{18}O	Blue	0	0	0/0	0/0	0/0	0/0
	Red	37	93	12/19	30/46	0.46/1.1	1.2/2.8
Combined ^d	Blue	10	25	13/20	32/50	2.7/6.2	6.3/15
	Red	152	378	110/170	271/422	14/33	34/82

Notes.

^a Blue (red) indicates all outflow emission at blueshifted (redshifted) velocities with respect to the cloud velocity, independent of position.

^b The values outside of the parentheses are with optical depth corrections, and those in parentheses are without such correction.

^c The values before the slash are not corrected for the outflow inclination and those after the slash are corrected assuming an inclination of 40° between the outflow axis and the plane of the sky.

^d Combining the ^{12}CO , ^{13}CO , and C^{18}O emission in different positions and velocity channels (see the main text for more detail).

in the first two rows of Table 1) are similar to those measured in Paper I with ALMA cycle 0 data. The correction of optical depth increases the mass estimation by a factor of about 8.5 for ^{12}CO . This increase is consistent with previous observations of other outflows (e.g., Dunham et al. 2014) and simulations (e.g., Offner et al. 2011; Bradshaw et al. 2015). The total momentum is increased by a factor of 4.9, and the total kinetic energy by a factor of 2.4 after the optical depth correction for ^{12}CO , suggesting that the momentum and kinetic energy are dominated by material at velocities higher than 4 km s^{-1} , where the ^{12}CO line becomes optically thin. Completing the ^{12}CO column density map with the slower material traced only by ^{13}CO and C^{18}O , the total mass of the redshifted outflow (last row of Table 1) is three times what is estimated using only opacity-corrected ^{12}CO , but the blueshifted outflow mass is similar. The combined total momentum is about 60% higher than that measured using only ^{12}CO . The kinetic energy estimated from the combined map is similar to that estimated from only ^{12}CO . Therefore, only using the opacity-corrected ^{12}CO emission may still underestimate the mass of the outflow by a factor of three due to the lack of the ability of ^{12}CO to trace the low-velocity components, but should represent a good estimate for the total momentum and the total kinetic energy.

With $T_{\text{ex}} = 15 \text{ K}$, the measured total mass of the CO outflow is $1.6 M_{\odot}$, the total momentum is $1.9 M_{\odot} \text{ km s}^{-1}$ (after correcting for inclination) and the total energy is $3.9 \times 10^{43} \text{ erg}$ (after correcting for inclination). The estimated mass and momentum of the CO outflow are significantly higher than those estimated from surveys, which give average outflow masses of $0.09 M_{\odot}$ for Class 0 sources and $0.06 M_{\odot}$ for Class I sources, and average outflow momenta of 0.7 and $0.3 M_{\odot} \text{ km s}^{-1}$ for Class 0 and I sources, respectively (e.g., Curtis et al. 2010). Similar low values were also given by Arce & Sargent (2006). With ^{13}CO used to correct for the ^{12}CO optical depth, Dunham et al. (2014) estimated the masses of 17 outflows from 0.01 to $0.8 M_{\odot}$ and their momenta from 0.02 to $3 M_{\odot} \text{ km s}^{-1}$. Our results are consistent with the highest mass and momentum they found, but higher than most of their sources. The main factor contributing to the differences between our results and previous estimates is including higher column density tracers to trace outflowing gas at low velocities (around 1 km s^{-1}). Our estimate of the outflow energy is similar to the previously

estimated values since the energy is dominated by less dense, high-velocity material traced by ^{12}CO . Note that our estimates of the outflow mass, momentum, and energy would be increased by a factor of 2.5 with the higher $T_{\text{ex}} = 50 \text{ K}$.

The measured mass of the redshifted outflow is 15 times higher than the mass of the blueshifted outflow. This again agrees with the very different environment of the two lobes. The momentum and kinetic energy of the red lobe are still higher than those of the blue lobe, but by a smaller factor, suggesting that even though much more material is entrained in the red lobe, the amount of material at high velocities is similar on both sides, which is also seen in Figures 11 and 12. We also see that the contrast between the two lobes is higher with a tracer of denser material (e.g., the contrast is higher in ^{13}CO than in ^{12}CO), suggesting there is more slower and denser material in the red lobe than in the blue lobe.

4. DISCUSSION

4.1. Role of the Outflow in Dispersing the Core

First, we study the question of whether the molecular outflow is entrained locally or entrained at small radii and then carried out. If most of the outflow material is entrained locally, we expect that the mass distribution of the outflow with respect to the distance from the central source is similar to the original mass distribution of the ambient material which filled the outflow cavity. The linear mass distribution of the outflow is calculated by integrating the mass surface density map of the outflow over semi-annuli centered at the central source (the annuli are shown in the top panel of Figure 11), which are shown in Figure 13 with red and blue lines for the red and blue lobes. To estimate the mass distribution of the ambient gas which was filling the outflow cavity, we assume the density profile of the original core is the same as that of the current remaining core. By fitting the sub-millimeter continuum emission, van Kempen et al. (2009) found that the remaining core has $5 M_{\odot}$ within 0.1 pc ($46'', 20,800 \text{ au}$) with the radial density profile following a power law $\rho \propto r^{-1.8}$. Therefore, we assume the original material distribution in the outflow cavity to be composed of a cone with a half-opening angle of 40° with the same density profile within $45''$ and a cylinder with a constant diameter and a constant density of 10^4 cm^{-3} from $45''$

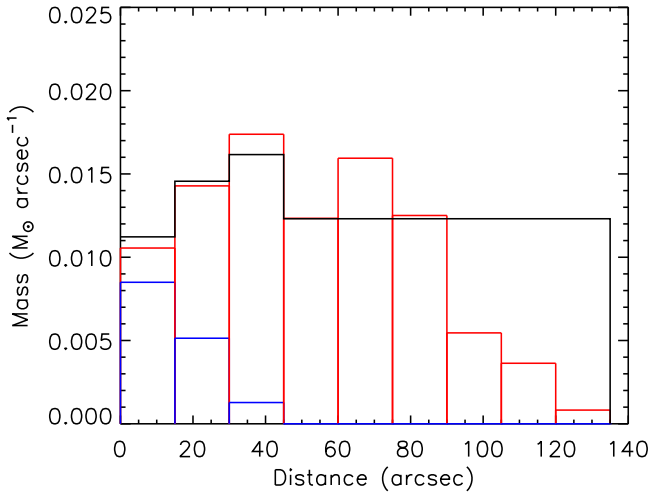


Figure 13. Mass distribution of the outflow with respect to the distance from the central source. The properties are integrated over several annuli shown in Figure 11. The red and blue curves represent the red lobe and the blue lobe. The black lines show the estimated mass distribution of the ambient material which originally filled the current outflow cavity.

to $120''$. The shape of this simplified outflow cavity is shown in the first panel of Figure 11. The density of 10^4 cm^{-3} for the outer part of the cloud is valid because C^{18}O and CS emission is detected throughout the region and it is consistent with the density profile for the inner core which gives $1.6 \times 10^4 \text{ cm}^{-3}$ at $45''$. van Kempen et al. (2009) also estimated the density of the outer cloud to be a few $\times 10^3 \text{ cm}^{-3}$ from detection of ^{12}CO (6-5) emission. The estimated mass distribution of the ambient material which was filling the outflow cavity is shown with black lines in Figure 13. The figure shows that the outflow mass distribution is, in general, at a level approximately similar to that of the mass distribution of the original core gas filling the outflow cavity, except in the regions close to the cloud edges (outermost two annuli of the blue and red lobes) where the outflow mass drops fast with the distance. This suggests that most of the outflow material is entrained locally from the ambient core, or not far from their current position, rather than being entrained close to the central source and then carried out. We note that, in the wide-angle wind entrainment model (see Section 4.2), the outflowing shell contains material accumulated all the way from the central source. However, in such a case, the “local entrainment” is still valid in the sense that the ambient material joins the outflow at its distance from the source, as opposed to infalling into the inner region first and then being launched and carried out. The wide-angle wind entrainment also mainly works at the base of the outflow, as shown in Section 4.2.

The above analysis implies that the core material becomes part of the outflow as the outflow cavity broadens. We then estimate the core destruction timescale based on this scenario of outflow broadening. Assuming that the core material is being entrained into the outflow at a constant rate, i.e., the solid angle extended by the outflow cavity increases at a constant rate, the core destruction timescale can be estimated to be $\tau_{\text{des}} = t_{\text{out}} / (1 - \cos \theta_c)$, where t_{out} is the current age of the outflow, and θ_c is the half-opening angle of the outflow cavity. For the central 0.1 pc core, the current outflow opening angle is approximately 40° , then the total core destruction time is $\tau_{\text{des}} = 4 t_{\text{out}}$. There are several ways to estimate the age of the

outflow. The dynamical age of the *molecular outflow* is not a reliable estimate of its true age since the outflow is entrained locally as discussed above. The dynamical age of the parsec-scale jet (Stanke et al. 1999) is about 9000 years, which is a lower limit since the jet could extend further. Instead, we use the typical age of an early Class I source as the age of this outflow, which is 0.13–0.26 Myr. This is estimated from the fact that the typical lifetime of the Class 0+I phase in low-mass star formation is 0.40–0.78 Myr, with about 1/3 of the time spent in the Class 0 phase (Dunham et al. 2014, 2015). The core destruction timescale is then approximately 0.52–1 Myr, which is consistent with the aforementioned Class 0+I lifetime. This timescale is also shorter than the collapsing timescale of the core (core mass divided by infall rate) which we estimate to be 1.5 Myr from the core mass of $5 M_\odot$ and the current infall rate of $3.2 \times 10^{-6} M_\odot \text{ yr}^{-1}$ estimated in Section 4.3. These suggest that the mass entrainment rate from the core to the outflow based on outflow broadening is high enough for the outflow to potentially disperse the core within the timescale of the embedded phase of low-mass star formation.

The formation efficiency from core to star is a key parameter for setting the final mass of the star, and it is believed to be strongly regulated by outflow feedback. In a simple scenario, as the protostar grows, the material in the core either accretes onto the star (with a small fraction onto the disk) or is entrained by the outflow. Some material can be expelled from the core by photoionizing winds, but this only becomes important for massive protostars. Therefore we can define three efficiencies: (1) the instantaneous efficiency

$$\epsilon(t) \equiv \frac{\dot{m}_*(t)}{\dot{m}_*(t) + \dot{m}_o(t)},$$

where \dot{m}_* is the accretion rate onto the protostar and \dot{m}_o is the rate at which the core material joins the outflow; (2) the current averaged efficiency,

$$\bar{\epsilon}(t) \equiv \frac{\int_0^t \dot{m}_* dt}{\int_0^t (\dot{m}_* + \dot{m}_o) dt} = \frac{m_*(t)}{m_*(t) + m_o(t)},$$

where $m_*(t)$ is the current protostellar mass and $m_o(t)$ is the current outflow mass; and (3) the final efficiency,

$$\bar{\epsilon}_f \equiv \bar{\epsilon}(t_f) = \frac{m_*(t_f)}{m_*(t_f) + m_o(t_f)} = \frac{m_{*f}}{M_c},$$

where t_f is the formation time, m_{*f} is the final mass of the protostar, and M_c is the initial mass of the core. For the instantaneous core-to-star efficiency, the protostellar accretion rate can be approximated by the infall rate of the innermost envelope, which is $3.2 \times 10^{-6} M_\odot \text{ yr}^{-1}$ (Section 4.3). On a similar scale (within $6''$), the outflow material with a velocity higher than the escaping velocity has a total momentum of $0.07 M_\odot \text{ km s}^{-1}$, which corresponds to an instantaneous mass loading rate of $0.07 M_\odot \text{ km s}^{-1} / 6'' = 5.5 \times 10^{-6} M_\odot \text{ yr}^{-1}$ for the outflow. The ratio between the infall rate and the outflow mass loading rate indicates the instantaneous core-to-star efficiency is about 1/3. For the current average core-to-star efficiency, by fitting the position–velocity (PV) diagrams of the ^{13}CO and C^{18}O flattened structure surrounding the central source, we find the dynamical mass of the central source is $0.3 M_\odot$ (see Section 4.3). Within $45''$ (i.e.,

the size of the $5 M_{\odot}$ core), the total outflow mass is $0.85 M_{\odot}$, and the total mass of the outflowing material with a velocity higher than the escape velocity is $0.6 M_{\odot}$, which is two to three times the mass of the protostars. This corresponds to a current average core-to-star efficiency of $1/3$ to $1/4$. These estimates of current core-to-star efficiencies are consistent with the final efficiencies estimated from observations of CMF and IMF or results of theoretical simulations (e.g., Federrath et al. 2014; Offner & Arce 2014). Thus, it appears that the outflow is already significantly influencing the star formation efficiency toward the driving protostar of the HH46/47 outflow.

4.2. Mechanisms of Outflow Entrainment

In Paper I, it was argued that the blueshifted outflow is mainly entrained by a wide-angle wind and the redshifted outflow is mainly entrained by the jet. Here we revisit the question of entrainment mechanism with the new ALMA data which has better angular resolution, recovers more of the extended emission, and includes more tracers.

Blueshifted outflow—the kinematics and morphology of the blueshifted outflow at velocities higher than about 6 km s^{-1} can be explained by a model in which the molecular outflow is swept up by a wide-angle wind. For a radial wind with force $\propto 1/\sin^2(\theta)$ interacting with a flattened ambient core with density $\propto \sin^2(\theta)/r^2$ and instantaneously mixing with shocked ambient gas, the swept-up shell is a radially expanding parabola with a Hubble law velocity structure (Li & Shu 1996; Lee et al. 2000). Following the simple analytical description by Lee et al. (2000), the morphology of such an outflowing shell is described by a parabola in the form of $z = CR^2$, with the z -axis along the outflow axis and the R -axis perpendicular to it, and the velocities of the shell on the directions of z and R are described by $v_z = v_0 z$ and $v_R = v_0 R$. The free parameters in such a model are the inclination i between the outflow axis and the plain of the sky, C , and v_0 .

As shown in Figures 14 and 15, such a model successfully reproduces the features in the ^{12}CO PV diagrams along and perpendicular to the outflow axis and the ^{12}CO channel maps of the blueshifted outflow at velocities higher than about 6 km s^{-1} . Along the outflow axis, the PV diagram of the blueshifted outflow shows an inclined parabolic structure. Meanwhile in the PV diagrams perpendicular to the outflow axis, elliptical structures are seen. The channel maps at velocities $\leq -6 \text{ km s}^{-1}$ also show elliptical ring structures. All these features are well fitted with our simple analytical model. The parameters of the best-fit model are $i = 40^\circ \pm 1^\circ$, $C = 0.4 \pm 0.1 \text{ arcsec}^{-1}$, and $v_0 = 1.5 \pm 0.1 \text{ km s}^{-1} \text{ arcsec}^{-1}$. The uncertainties are the range of the values with which relatively good fits can be achieved by visual inspection. The fitted inclination of the outflow is consistent with the value derived from the observations of the optical jet by Eislöffel & Mundt (1994) and Hartigan et al. (2005), which is $34^\circ \pm 3^\circ$ and $37.5^\circ \pm 2.5^\circ$, respectively. The parameter v_0 corresponds to a timescale of $t_0 = 1/v_0 = 1.4 \times 10^3$ years, which can be considered as the dynamical age of the wide-angle wind-entrained outflow. This age is even shorter than the dynamical age of the jet (9000 years) and is certainly much shorter than the expected age for an outflow driven by an early Class I source ($\text{several} \times 10^5$ years; see discussion in Section 4.1). This suggests that the wide-angle wind entrainment has started to become visible or began to be visible only very recently.

The very young age of the wide-angle wind-entrained outflow is consistent with the fact that the majority of the blueshifted outflow emission is at lower velocities and not following the prediction of the wide-angle wind model. At a lower velocity, the emission is concentrated along the parabolic outflow cavity walls (see Figure 4), which may be the material that was entrained before and has slowed down while interacting with the remaining core. Jet bow-shock entrainment, even though there is no clear evidence left in the morphology or kinematics of the emission, could still be responsible for entraining this material in the past, considering an optical jet is seen inside the blueshifted outflow cavity. The fitted power-law index of the mass–velocity relationship of the blueshifted outflow (Figure 12, Section 3.7) is more consistent with the jet bow-shock entrainment model, which predicts $-3.5 < \gamma < -1.5$, than the wide-angle wind-entrainment model, which predicts $-1.8 < \gamma < -1.3$ (e.g., Lee et al. 2001). In fact, fitting a power law for the high-velocity portion ($|v_{\text{out}}| > 6 \text{ km s}^{-1}$) gives an index of $\gamma = -1.27$, consistent with the wide-angle wind model, and fitting a power law for the low-velocity portion ($|v_{\text{out}}| < 6 \text{ km s}^{-1}$) gives an index of $\gamma = -3.74$, which is more consistent with the jet bow-shock model. This again suggested the idea that two entrainment mechanisms co-exist in the blueshifted outflow.

Redshifted outflow—the kinematics and morphology of the redshifted outflow show evidence of jet bow-shock entrainment. Figure 14 shows that the three ^{12}CO clumps R1, R2, and R3 on the redshifted outflow axis have distinctive kinematic features that the velocity increases with the distance to the central source. This type of feature is generally called “Hubble wedges,” and is considered to be produced by the entrainment of ambient gas by the jet bow-shock (Arce & Goodman 2001a). The three ^{12}CO clumps are also coincident with the shocked region shown as bright IR or optical knots along the redshifted outflow axis (Figure 16, upper panel), or at same distances with respect to the central source as the bright knots in the blueshifted optical jet, which also trace shocks. Therefore the ^{12}CO clumps R1, R2, and R3 mark the positions of the apices of three bow shocks produced by episodic mass ejection, as argued in Paper I.

The three ^{12}CO clumps are connected with the outflow cavity walls by diffuse emission, following bow-shock shapes (Figure 14, top panel). More careful inspection reveals that the northern outflow cavity wall is actually composed of multiple shells associated with these bow shocks. As mentioned in Section 3.2, two or more parallel thin structures can be identified in the northern wall of the outflow cavity from about $30''$ from the central source to the end of the red lobe in the channel maps at velocities from 1.8 to 3.6 km s^{-1} . The inner layer of the cavity wall deviates from the outer layer and curves toward clump R2 on the axis at a distance of about $90''$ from the central source, while the outer layer extends further out.

We can also identify these different layers in the outflow cavity wall in the PV diagrams. Figure 17 shows the PV diagram perpendicular to the outflow axis at several positions along the red lobe. The PV diagram in the C9 cut shows that the northern outflow cavity wall is composed of three components at distances of approximately $5''$, $10''$, and $18''$ from the axis (marked with red arrows). Each of these components has an emission peak and wider velocity range than the emission between them. Such structures are seen consistently over the redshifted outflow as shown in Figure 17.

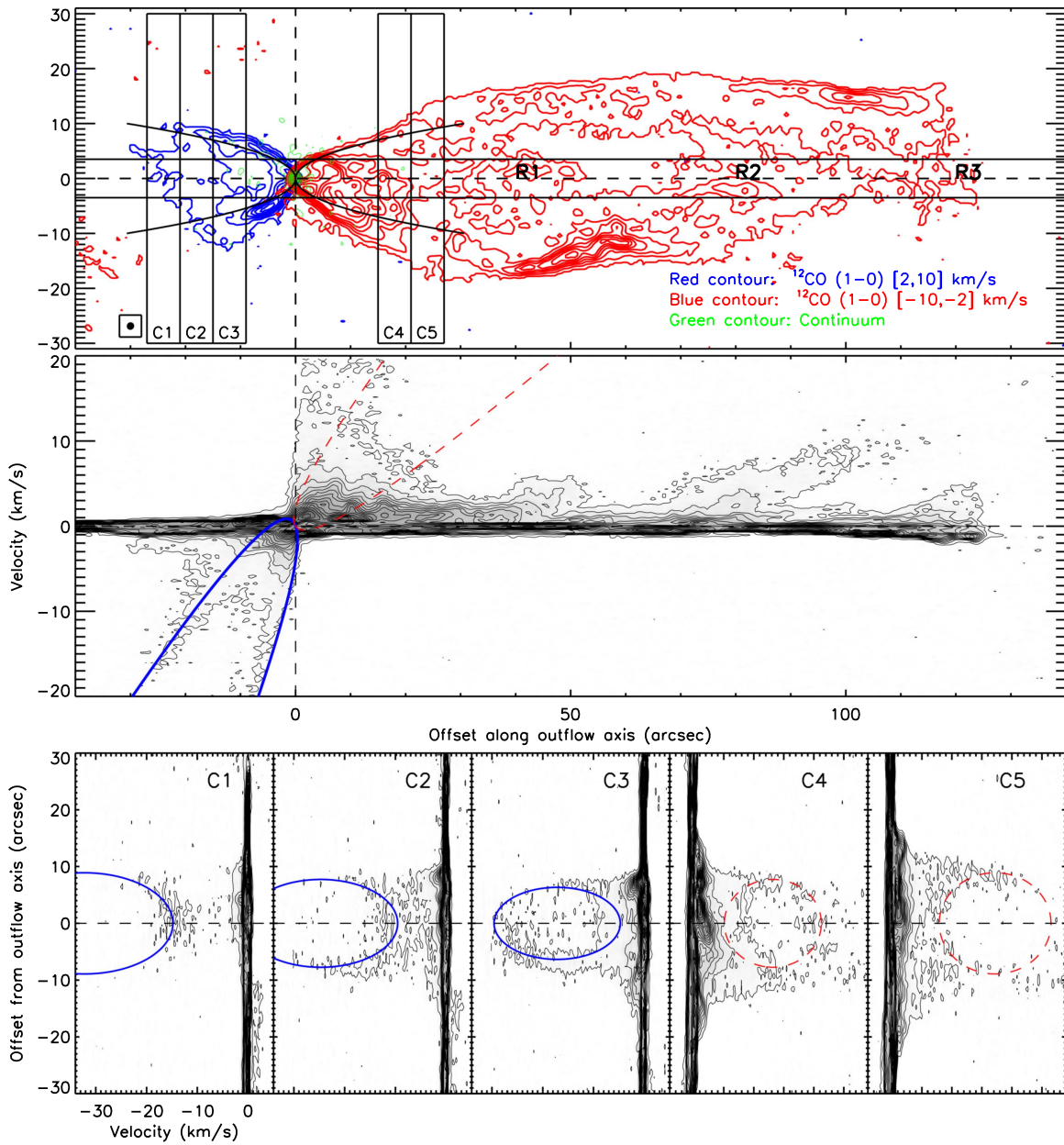


Figure 14. Top: ^{12}CO (1–0) emission integrated from 2 to 10 km s^{-1} shown in the red contours, and emission integrated from –10 to –2 km s^{-1} shown in the blue contours. The images are rotated by 30° counterclockwise. The contours start at 3σ with a step of 6σ ($1\sigma = 21 \text{ mJy beam}^{-1} \text{ km s}^{-1}$). The rectangles show the cuts for the PV diagrams shown in the panels below. The parabolas show the projected shape of the model outflow cavity. Middle: the position–velocity diagram of ^{12}CO (1–0) along the outflow axis with a cut width of $7''$. The contours start at 38 mJy beam^{-1} with a step of 38 mJy beam^{-1} . The blue and red curves show the PV diagrams from a model where outflow shells are driven by a wide-angle wind (see Section 4.2). Bottom: position–velocity diagrams of ^{12}CO (1–0) along $6''$ wide cuts perpendicular to the outflow axis. The contours start at 36 mJy beam^{-1} with a step of 36 mJy beam^{-1} . The blue and red ellipses show the model fit.

At a further distance from the source (cut C10), the innermost components of the northern outflow cavity wall seen in the cut C9 move toward the axis and start to merge with the emission of clump R2. At a distance closer to the central source (cut C8), this inner component is further away from the axis.

The different shells are also seen in different velocities and tracers. In the upper panel of Figure 16, close to the end of the outflow cavity, the high-velocity emission follows the infrared emission and curves to the outflow axis, tracing the bow-shock whose apex is at the end of the IR outflow cavity (i.e., the ^{12}CO clump R3). On the other hand, part of the low-velocity emission remains parallel to the outflow axis and deviates from the IR emission, suggesting it may be material entrained by

bow shocks which have already moved out of the cloud, which is consistent with the fact that the jet extends to a parsec-scale distance. In the lower panel of Figure 16, most of the low-velocity ^{13}CO and CS emission trace a closed outflow cavity structure which ends around the position of the R2 clump, while some of the ^{13}CO emission extends further away to the position of clump R3.

All these features suggest that the extended redshifted outflow (with distance $\gtrsim 30''$ from the central source) is composed of several nested shells formed by entrainment of a series of jet bow shocks. Such a scenario is consistent with theoretical models of jet bow-shock entrainment (e.g., Raga & Cabrit 1993; Lee et al. 2001) and is also supported by recent

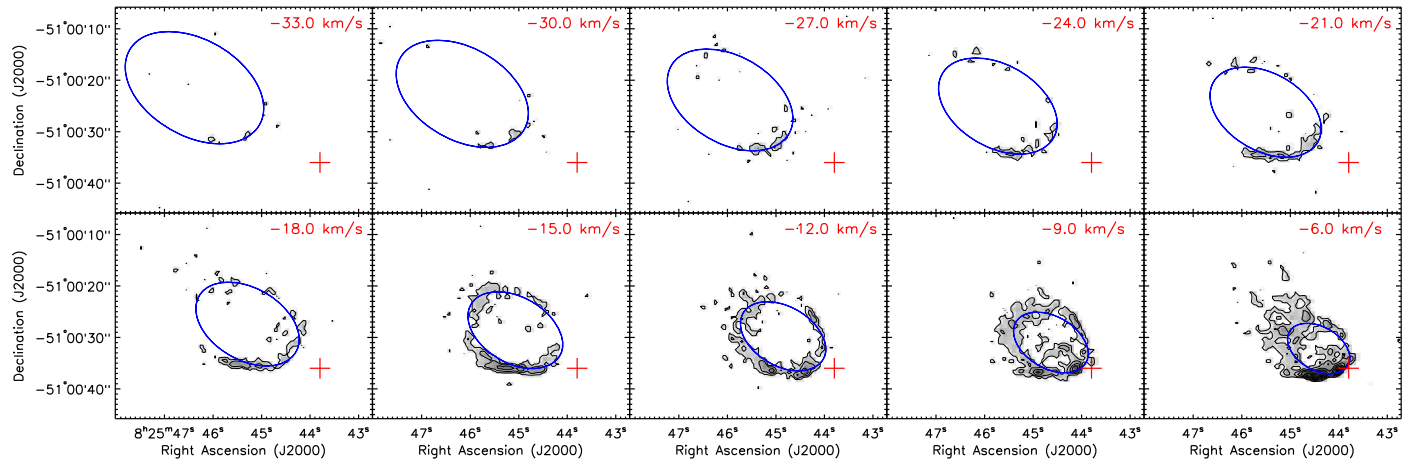


Figure 15. Channel maps of the ^{12}CO (1–0) emission at velocities less than or equal to -6 km s^{-1} showing the blueshifted outflow. The channel width is 3 km s^{-1} . The contours start at 3σ with a step of 6σ ($1\sigma = 4.5 \text{ mJy beam}^{-1}$). The synthesized beam is $1''.35 \times 1''.30$ (P.A. = -55.2°). The red crosses mark the central source (peak of the continuum emission). The blue ellipse in each panel shows the expected shape of emission from the model where outflow shells are driven by a wide-angle wind (see Section 4.2).

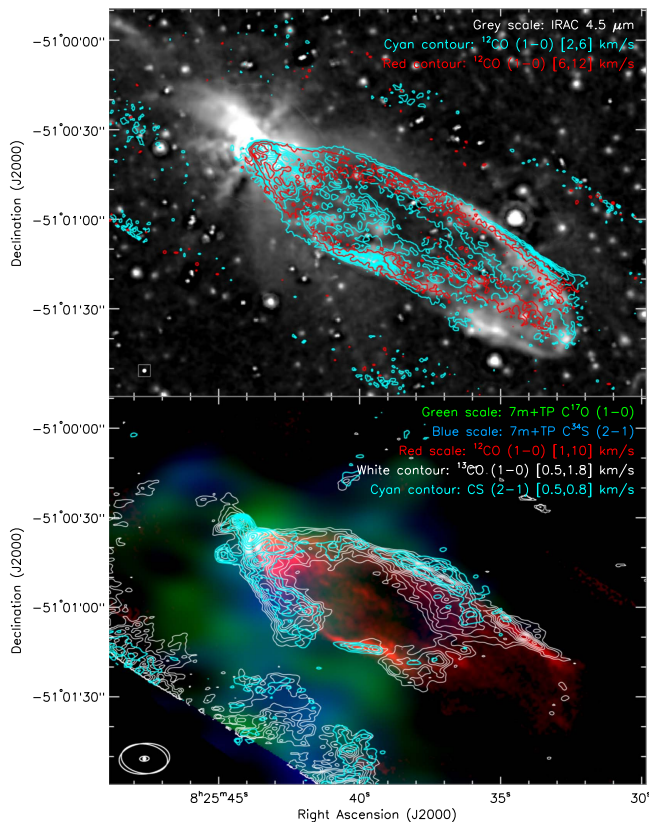


Figure 16. Upper panel: comparison of the redshifted CO outflow with the *Spitzer* IRAC $4.5 \mu\text{m}$ image. The *Spitzer* data are from Noriega-Crespo et al. (2004) and have been reprocessed with a deconvolution algorithm to reach an angular resolution of about $0''.6$ – $0''.8$, with 60 iterations (see Noriega-Crespo & Raga 2012 for details). The cyan and red contours show the ^{12}CO emission integrated from 1 to 6 km s^{-1} and from 6 to 12 km s^{-1} , respectively. The lowest contour and subsequent contour steps are 3σ and 6σ ($1\sigma = 15 \text{ mJy beam}^{-1} \text{ km s}^{-1}$ for the cyan contours and $1\sigma = 19 \text{ mJy beam}^{-1} \text{ km s}^{-1}$ for the red contours). Lower panel: the redshifted outflow cavity traced by ^{12}CO , ^{13}CO , and CS. The red color scale shows the integrated emission of ^{12}CO (1–0) from 1 to 10 km s^{-1} . The white and cyan contours show the ^{13}CO (1–0) emission integrated from 0.5 to 1.8 km s^{-1} and the CS (2–1) emission integrated from 0.5 to 0.8 km s^{-1} . The lowest contour and subsequent contour steps are 6σ and 3σ , respectively ($1\sigma = 6.4 \text{ mJy beam}^{-1} \text{ km s}^{-1}$ for white contours and $1\sigma = 2.2 \text{ mJy beam}^{-1} \text{ km s}^{-1}$ for cyan contours). The integrated emission of ^{17}O (1–0) and ^{34}S (2–1) are also shown for reference in green and blue color scales, respectively.

observations in other sources (e.g., HH212, Lee et al. 2015). Here with the unprecedented angular resolution and sensitivity of ALMA, we not only identify the shells around the apices of the bow shocks but also resolve them in the outflow cavity walls.

However, at the base of the outflow cavity, the wide-angle wind may still contribute. For example, Figure 14 shows that some of the PV diagrams perpendicular to the outflow axis also show elliptical rings (lower panel, cut C4 and C5) similar to those seen on the blue lobe at the same distances to the central source. The red dashed ellipses in the figure show the fits to these features using the wide-angle wind-entrainment model described above, with the same inclination i and outflow cavity shape C , but a slower velocity, $v_0 = 0.8 \text{ km s}^{-1} \text{ arcsec}^{-1}$. However, we do not find clear evidence of a wide-angle wind-entrained outflow in the PV diagram along the outflow axis, although some of the high-velocity emission close to the central source seems to be consistent with such a model. Also the ^{12}CO channel maps do not show the ring structures expected by the wide-angle wind model as in the blueshifted outflow. We also see a wider structure at the base of the redshifted outflow which can be evidence of a wide-angle wind. It is most clearly seen in the ^{12}CO channel maps at velocities from 0.6 to 2.1 km s^{-1} , especially toward the south of the central source. A similar, but even wider structure appears in low-velocity ^{13}CO and CS emission (Figure 16, lower panel). Spatially these coincide with the diffuse emission in the IRAC $4.5 \mu\text{m}$ continuum images (Figure 16, upper panel). These extended IR emissions were argued to be scattered light by an outflow cavity wider than that in IR shock emissions (Velusamy et al. 2007). Therefore the structure in low-velocity CO and CS emission may be tracing the outflowing material in this wider cavity, which is entrained by a wide-angle wind. At a larger polar angle from the outflow axis, the wide-angle wind is slower and therefore the entrained material only appears in the low-velocity range. In addition, as discussed in Section 3.7, the energy map of the outflow (Figure 11, lower panel) shows that, in the red lobe, the kinetic energy is concentrated at the base of the outflow cavity, which is not consistent with a jet bow-shock entrainment scenario in which most of the energy is expected to be injected at the heads

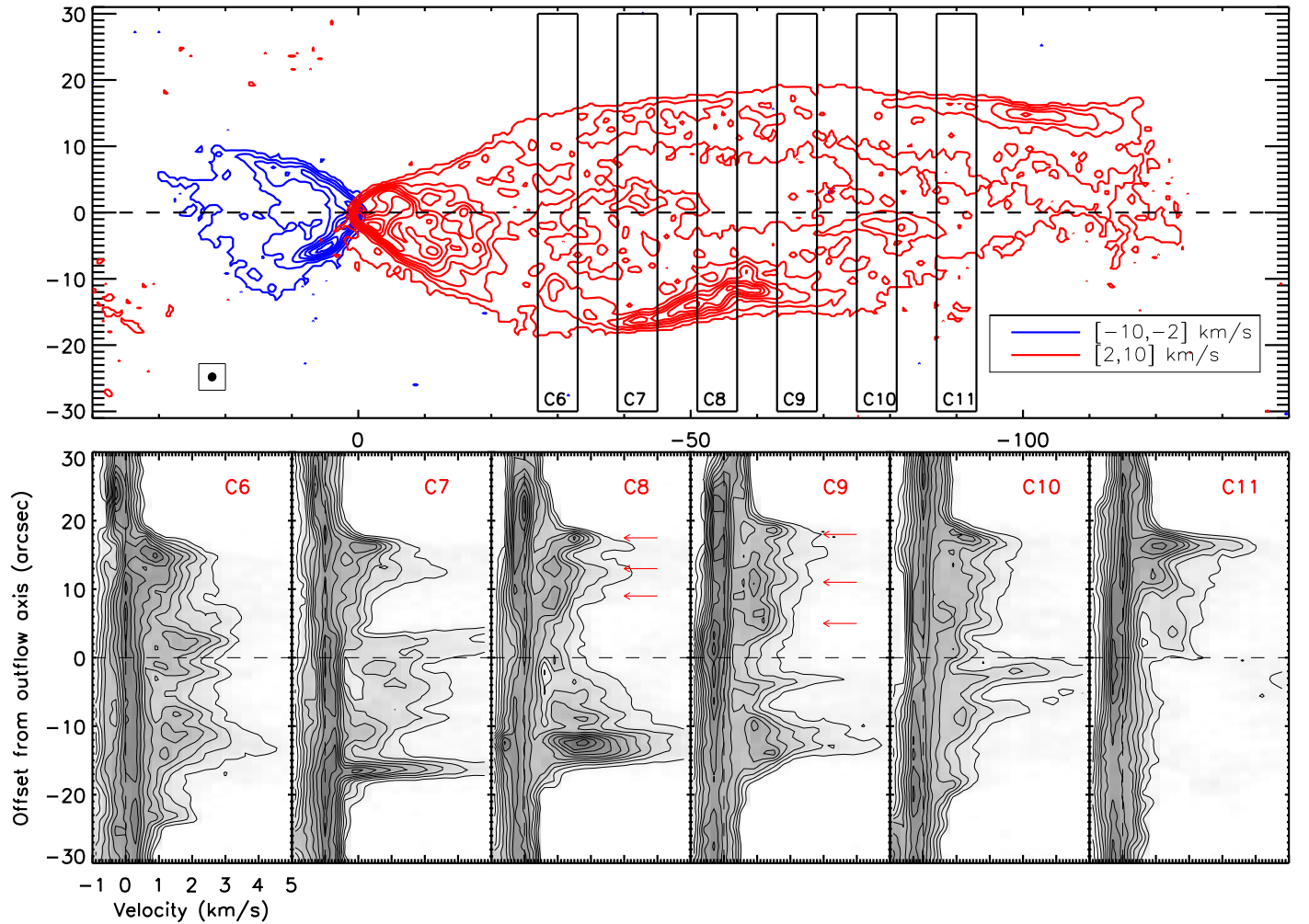


Figure 17. Upper panel: integrated intensity maps of the ^{12}CO red and blueshifted outflow lobes (the same as the top panel of Figure 14). Lower panel: the position-velocity diagrams of ^{12}CO (1–0) along 6'' wide cuts perpendicular to the outflow axis. The contours start at 36 mJy beam⁻¹ with a step of 36 mJy beam⁻¹.

of bow shocks, suggesting a second entrainment mechanism (such as wide-angle wind) is in action.

To summarize, we find evidence that jet bow-shock entrainment and wide-angle wind entrainment co-exist in both the blueshifted and redshifted outflows, although which mechanism is more visible differs on the two sides. While the blueshifted outflow cavity has been cleared and little material is along the jet path, making the wide-angle wind entrainment apparent, the redshifted outflow cavity has a large amount of remaining dense material resulting in significant jet bow-shock entrainment in this region. Since the outflow cavity is gradually cleared as a protostar evolves, we would expect to see the jet entrainment is more visible in an earlier stage while the wide-angle wind becomes visible in a later stage. We note that the jet and wide-angle wind do not need to be two distinct wind types; rather they can be two components of a single wind from the accretion disk with its density and/or velocity depending on the polar angle from the outflow axis (e.g., Cabrit et al. 1999; Shang et al. 2006).

4.3. Rotational Structure Around the Central Source

As mentioned in Sections 3.3 and 3.4, velocity gradients are found across the central source perpendicular to the outflow axis in both ^{13}CO and C^{18}O , indicating a rotating structure

around the central source. In Figures 18 and 19, the ^{13}CO and C^{18}O integrated emissions show a flattened structure around the central source with its major axis perpendicular to the outflow axis. Its size is about 10'' (4500 au) across, which is much larger than what is expected for a rotationally supported Keplerian disk (typically a few hundred au for Class 0 and I sources; e.g., Yen et al. 2013). Therefore it is likely to be a rotating envelope that feeds the accretion disk which we are not able to resolve with our current data. The morphology of this flattened structure is affected by the outflow. On the blueshifted side, its boundary outlines the outflow cavity. On the redshifted side, the brightest part of the flattened structure bends following the redshifted outflow cavity. The peaks of the ^{13}CO and C^{18}O integrated emissions are close to the continuum peak. The most extended continuum emission is elongated in the north–south direction, consistent with the brightest parts of the ^{13}CO and C^{18}O emissions.

The upper right panel of Figure 18 shows the PV diagram of ^{13}CO along the major axis of the flattened structure (i.e., perpendicular to the outflow axis). In addition to the two major components within a distance of about 6'' from the central source, there is emission at -1 to -0.5 km s^{-1} and at 0.5 km s^{-1} at a position between -8 and $-12''$ from the center. The blueshifted emission across this region is associated with the larger cloud structure at this velocity (see Figure 5), and the

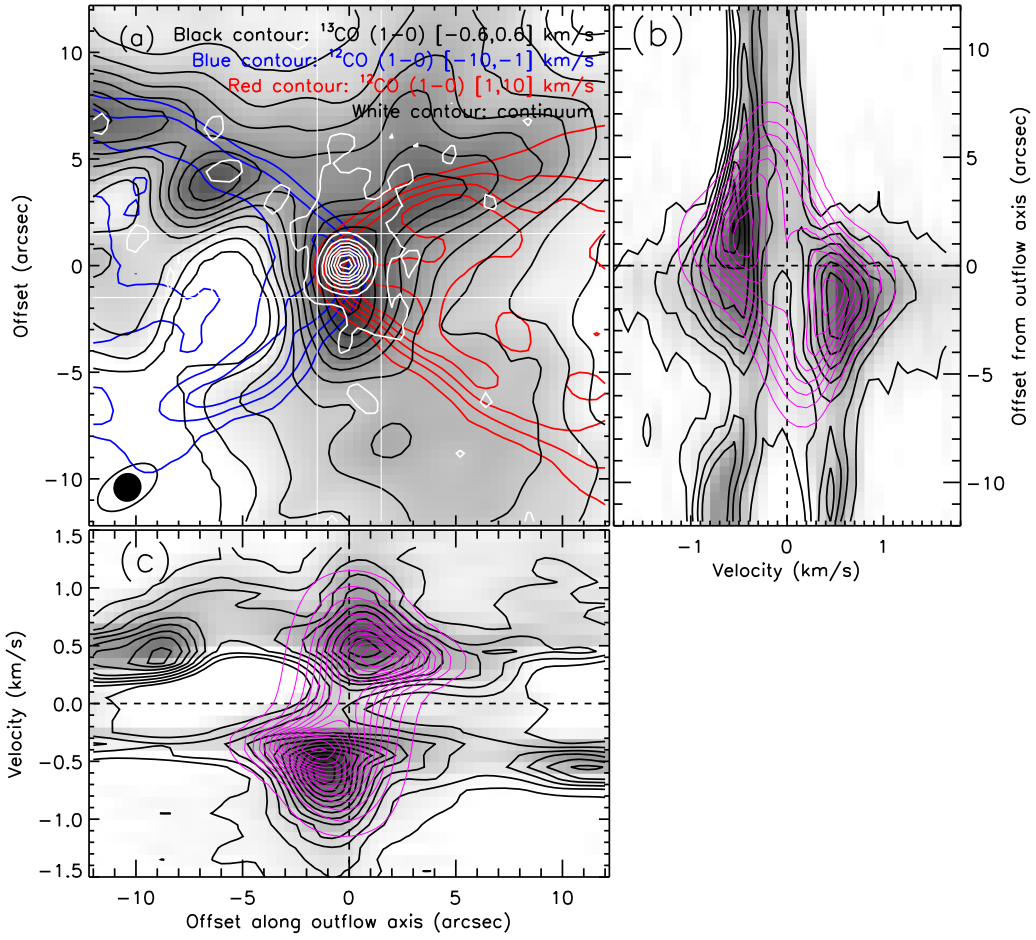


Figure 18. (a) ^{13}CO emission integrated from -0.6 to 0.6 km s^{-1} (gray scale and black contours) showing the envelope. Only the interferometric data are used. The contours start from 3σ with a step of 6σ ($1\sigma = 6.2 \text{ mJy beam}^{-1} \text{ km s}^{-1}$). The red and blue contours show the redshifted (1 to 10 km s^{-1}) and blueshifted (-10 to -1 km s^{-1}) ^{12}CO outflows for reference. The white contours, which show the continuum emission, start at 3σ and have a step of 15σ ($1\sigma = 0.04 \text{ mJy beam}^{-1}$). The images are rotated counterclockwise by 30° so that the outflow axis lies along the x -axis. The white stripes show the cuts used for the PV diagrams. (b) The position-velocity diagram of ^{13}CO ($1-0$) along the $3''$ wide cut perpendicular to the outflow axis (black contours and gray scale). The purple contours show the PV diagram expected from a model including infall and rotation. Both black and purple contours start at 36 mJy beam^{-1} with a step of 72 mJy beam^{-1} . (c) Same as panel (b) but along the outflow axis. The contours start at 24 mJy beam^{-1} with a step of 48 mJy beam^{-1} .

redshifted component is separated from the central flattened structure and appears to come from the outflow. Therefore we only focus on the two main components within $6''$ of the center on the PV diagram. At higher velocities, the emission is confined near the central source (i.e., within $2''$), while at lower velocities the emission extends to the north and south of the source. Although the blueshifted and redshifted emission peaks lie on different sides of the central source, the fainter emission is more symmetric. The PV diagram clearly shows a signature of rotation around the central source, but the high-velocity emission across the rotation axis suggests there is also infall or outflow motion involved. The lower left panel of the same figure shows the PV diagram of ^{13}CO along the minor axis of this flattened structure (i.e., along the outflow axis). We also can identify two main components showing a velocity gradient along the direction of the outflow axis, which again indicates that infall or outflow motion exists in addition to rotation. Figure 19 shows similar features for the C^{18}O flattened envelope.

We compare the observed PV diagrams with a simple analytic model similar to those used by Ohashi et al. (1997) and Lee et al. (2006). In this model, the rotation velocity is assumed to be inversely proportional to the radius, therefore conserving angular momentum, $v_{\text{rot}} = j/R$, and the infalling velocity is then

$v_{\text{infall}} = \sqrt{2Gm_*/R - (j/R)^2}$ as imposed by mechanical energy conservation in the potential well of the central source (e.g., Sakai et al. 2014). The envelope extends from the centrifugal barrier radius where all kinetic energy is converted to the rotational motion $R_{\text{in}} = j^2/(2Gm_*)$ to an outer radius R_{out} with a constant thickness of H . The density and temperature distributions follow power laws $n \propto R^{-k_p}$ and $T = T_{1000 \text{ au}}(R/1000 \text{ au})^{-k_T}$, where $T_{1000 \text{ au}}$ is the temperature at $R = 1000 \text{ au}$. Such a model has nine parameters j , m_* , R_{out} , H , k_p , m_{env} , k_T , $T_{1000 \text{ au}}$, and inclination i , where the mass of the envelope m_{env} , together with R_{out} and H , is used to set the density. We try to use a single set of the parameters to reproduce both the ^{13}CO and C^{18}O PV diagrams. To narrow our search, we fix $R_{\text{out}} = 6''$ (2700 au) from the current observation, and $k_p = 1.8$ from the observation by van Kempen et al. (2009). The temperature is assumed to follow the dust temperature profile by heat from a $12 L_\odot$ protostar (Equation (2) in Motte & André 2001), with $k_T = 0.4$ and $T_{1000 \text{ au}} = 25 \text{ K}$. The purple contours in Figures 18 and 19 show an example of our model. The fitted parameters are the specific angular momentum $j = 1 \text{ arcsec km s}^{-1}$ (450 au km s^{-1}), the dynamical central mass $m_* = 0.3 M_\odot$, the envelope mass $m_{\text{env}} = 0.1 M_\odot$, the envelope thickness $H = 1''$ (900 au), and the inclination between the line of sight and the envelope mid-plane $i = 30^\circ$.

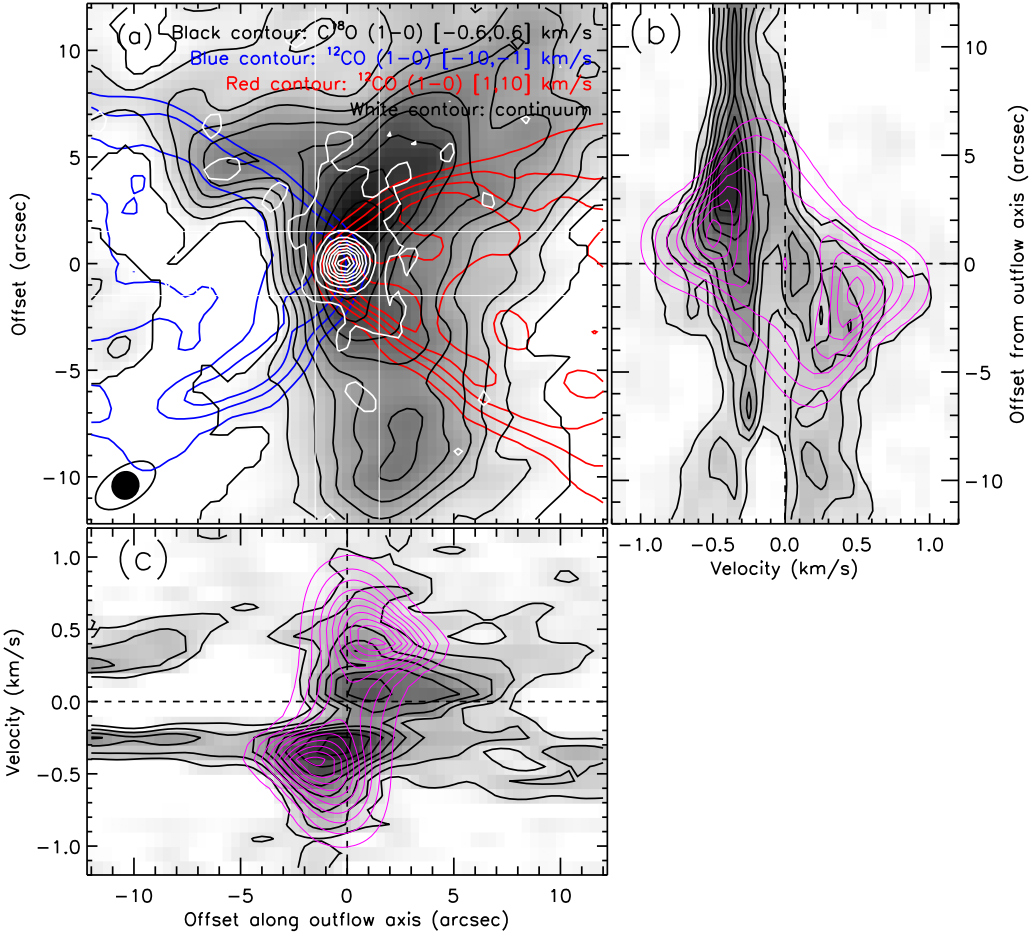


Figure 19. (a) Same as Figure 18(a), but with the gray scale and black contours showing the C^{18}O emission integrated from -0.6 to 0.6 km s^{-1} . The contours start from 3σ with a step of 3σ ($1\sigma = 5.6 \text{ mJy beam}^{-1} \text{ km s}^{-1}$). (b) Same as Figure 18(b), but for C^{18}O . Both black and purple contours start at 33 mJy beam^{-1} with a step of 33 mJy beam^{-1} . (c) Same as Figure 18(c), but for C^{18}O . The contours start at 27 mJy beam^{-1} with a step of 27 mJy beam^{-1} .

We are not performing a detailed model fit here, but rather we aim to show that the observed PV diagrams of the flattened structure are consistent with a collapsing envelope with rotation. The model reproduces most of the features in the PV diagrams, including the velocities, positions, and intensities of the emission peaks, and the different behaviors of the emissions at high and low velocities. However, the observation shows emission more spread out in space than the model. We also note that the emission peaks in the C^{18}O PV diagram along the minor axis of the envelope are not symmetric in velocity, which may be caused by the outflow.

Better agreement between the model and the observation can be achieved if we use different parameters for ^{13}CO and C^{18}O . The PV diagrams of ^{13}CO can be better fitted with $j = 1.2 \text{ arcsec km s}^{-1}$ and $m_* = 0.4\text{--}0.5 M_\odot$, and the PV diagrams of C^{18}O can be better fitted with $j = 1 \text{ arcsec km s}^{-1}$ and $m_* = 0.2 M_\odot$. The differences between these models can be considered the uncertainties of these parameters. Compared with the parameters describing the dynamics (j, m_*), the parameters that describe the geometry or density distribution (H, m_{env}) are less well constrained. The inclination of the model envelope, which is mainly constrained by the position separation of the emission peaks on the two PV diagrams, differs from the outflow inclination (Section 4.2). These all suggest that the geometry or density/temperature distribution of the envelope in this model is over-simplified. Note that here

we neglect the effect of CO depletion, which is expected at temperature $\lesssim 20 \text{ K}$ in protostellar envelopes (e.g., Zhang & Tan 2015), which happens at about $R = 1800 \text{ au}$ ($4''$) for the temperature profile we adopt. Therefore it is likely that we have underestimated the envelope mass.

From the estimated specific angular momentum j and the central mass m_* , the corresponding centrifugal barrier radius is $R_{\text{in}} = 0''.85$ (380 au), which can be considered the outer radius of a rotationally supported Keplerian disk. This size is at the high end of typical Class 0 and I disks (Harsono et al. 2014). The mass of the envelope $m_{\text{env}} = 0.1 M_\odot$ is consistent with the mass traced by ^{13}CO ($0.09 M_\odot$ with $T_{\text{ex}} = 15 \text{ K}$) and C^{18}O ($0.1 M_\odot$ with $T_{\text{ex}} = 15 \text{ K}$) within a $12'' \times 6''$ rectangle centered on the central source, using only the interferometric data. This mass is likely a lower limit of the envelope mass since CO may be depleted in the cold region. On the other hand, the dust mass of $0.3 M_\odot$ estimated from the continuum emission (Section 3.1) provides an upper limit of the envelope mass, since a large fraction of the continuum emission is from the central peak which may trace the unresolved disk rather than the infalling envelope. From j and m_* estimated above, the infall velocity is 0.41 km s^{-1} at a distance of $6''$ (2700 au). We then estimate the infall rate to be $\dot{m}_{\text{infall}} = m_{\text{env}} v_{\text{infall}} / R = 3.2 \times 10^{-6} M_\odot \text{ yr}^{-1}$ with $m_{\text{env}} = 0.1 M_\odot$. Note that the infall rate here is still a lower limit because of the neglect of CO depletion. Hartigan et al. (1994) estimated the mass loading rate of the jet to be

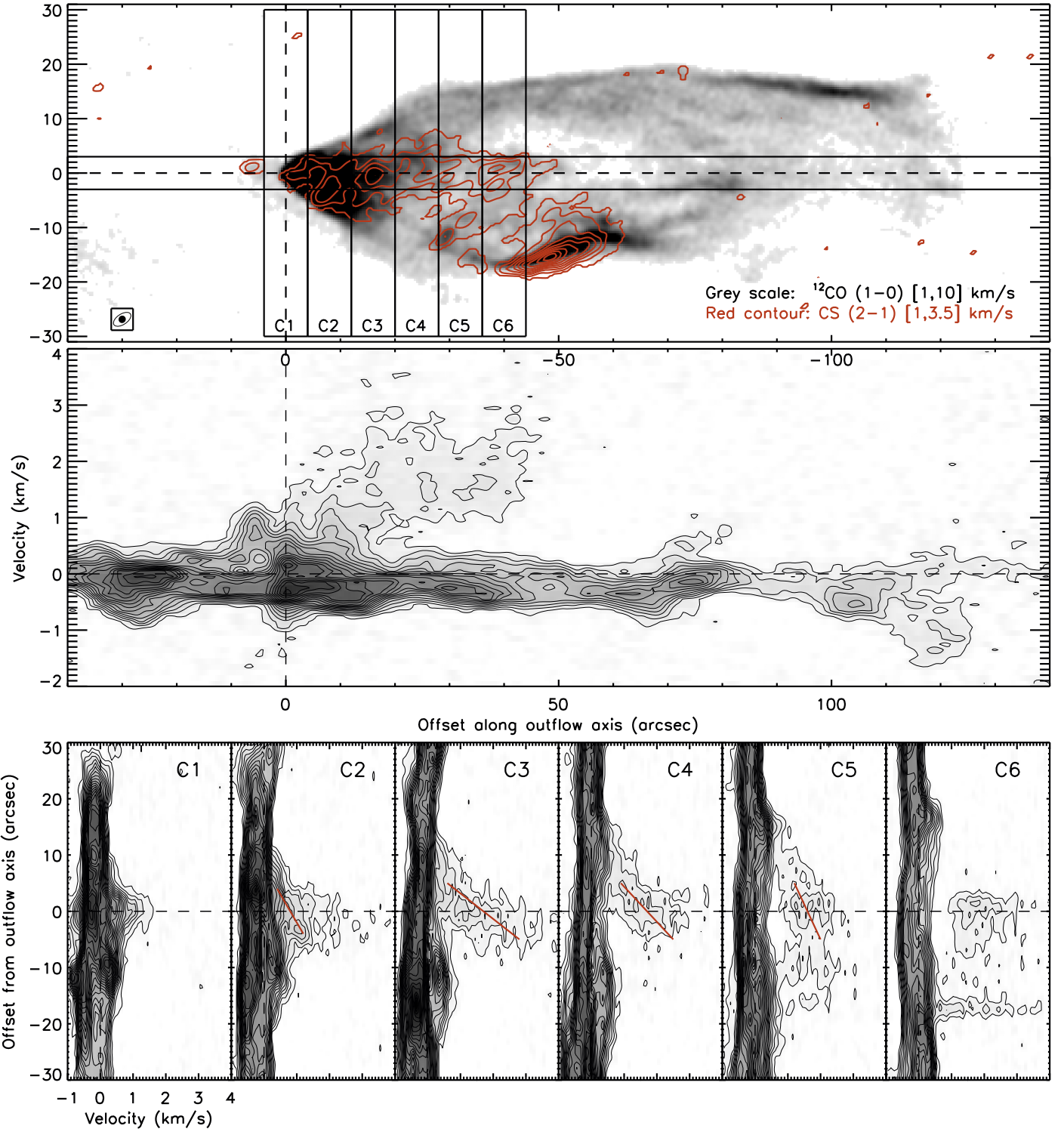


Figure 20. Top: CS (2–1) emission integrated from 1 to 3.5 km s^{-1} relative to the cloud velocity shown in red contours overlaid on ^{12}CO (1–0) image integrated from 1 to 10 km s^{-1} in gray scale. The images are rotated by 30° counter-clockwise. The contours start at 3σ with a step of 3σ with $1\sigma = 6.5 \text{ mJy beam}^{-1} \text{ km s}^{-1}$. The cuts for the PV diagrams are shown. Middle: position–velocity diagram of CS (2–1) along the outflow axis with a cut width of 6''. The contours start at 48 mJy beam^{-1} with a step of 48 mJy beam^{-1} . Bottom: position–velocity diagrams of CS (2–1) along 8''-wide cuts perpendicular to the outflow axis. The contours start at 36 mJy beam^{-1} with a step of 36 mJy beam^{-1} . The red lines indicate the velocity gradients across the outflow axis.

$4 \times 10^{-7} M_{\odot} \text{ yr}^{-1}$, which leads to an accretion rate of about $4 \times 10^{-6} M_{\odot} \text{ yr}^{-1}$ assuming that the accretion rate is 10 times higher than the jet mass loading rate (e.g., Ellerbroek et al. 2013 and references therein). The envelope infall rate estimated above is high enough to feed this accretion rate.

4.4. Rotating Outflow

Figure 20 shows that in the velocity range from 1 to 3.5 km s^{-1} the CS (2–1) emission appears to trace a collimated structure along the axis of the redshifted outflow (top panel). This jet-like structure starts at the position of the central source

and extends to about $50''$ (22,000 au) along the outflow axis where most of the ^{12}CO emission inside the outflow cavity ends with the R1 clump and a bright H_2 knot. The PV diagram along the axis (Figure 20, middle panel) shows that the velocity increases with the distance to the central source, indicating jet bow-shock entrainment as discussed in Section 4.2. The coincidence of the CS and ^{12}CO emission suggests that CS is tracing the same material entrained by the jet bow-shock which has an apex at the ^{12}CO clump R1.

The PV diagrams perpendicular to the outflow axis (Figure 20, bottom panel) show that there are consistent velocity gradients perpendicular to the outflow axis from $8''$ to $32''$ with respect to the central source and the gradient is highest at about $16''$ from the central source. One possible explanation of this gradient is outflow rotation, considering the direction of the velocity gradient is consistent with the rotation of the flattened envelope around the central source (see Section 4.3). We admit that this is only a tentative evidence of outflow rotation. Another possibility is that the emission is part of ring-like structures on PV diagrams which can be produced by the jet bow-shock entrainment (Lee et al. 2000). However, in such cases the highest velocity gradient is expected to be at the apex of the jet bow-shock, which is not seen here. The other possibilities include asymmetric shock interaction or jet precession.

If outflow rotation is the case, the projected rotational velocity is $0.4\text{--}1.1 \text{ km s}^{-1}$ with a mean value of 0.7 km s^{-1} (the velocity differences between the ends and the mid-points of the red lines in Figure 20) at a radius of about $4''$ (1800 au) from the outflow axis (the distance between the ends of the red lines and the outflow axis shown in Figure 20). The specific angular momentum is then $j_{\text{CS}} \approx 1600 \text{ au km s}^{-1}$ using the above radius and mean rotational velocity (0.9 km s^{-1} after correcting for the inclination of 40° of the outflow). Assuming the transport of angular momentum from a jet to its entrained outflow is on the same level as the jet's linear momentum transport, the jet that has entrained the CS outflow should have a specific angular momentum

$$j_w = j_{\text{CS}} \left(\frac{v_{p,w}}{v_{p,CS}} \right) \approx 1600 \left(\frac{v_{p,w}}{v_{p,CS}} \right) \text{ au km s}^{-1}, \quad (6)$$

where $v_{p,w}$ is the poloidal velocity of the jet, and $v_{p,CS}$ is the poloidal velocity of the CS outflow (around 3.5 km s^{-1} after correcting for the inclination). We then can estimate the launching radius of this wind using the formula provided by Anderson et al. (2003) (Equation (5) of their paper),

$$\varpi_0 = 0.7 \text{ au} \left(\frac{j_w}{100 \text{ au km s}^{-1}} \right)^{2/3} \times \left(\frac{v_{p,w}}{100 \text{ km s}^{-1}} \right)^{-4/3} \left(\frac{m_*}{1 M_\odot} \right)^{1/3}, \quad (7)$$

which combined with Equation (6) yields

$$\varpi_0 = 62 \text{ au} \left(\frac{v_{p,w}}{30 \text{ km s}^{-1}} \right)^{-2/3} \left(\frac{m_*}{0.3 M_\odot} \right)^{1/3}. \quad (8)$$

We can further deduce the magnetic lever arm following Ferreira et al. (2006) (Equation (10) of their paper) to be

$$\lambda = 106 \left(\frac{v_{p,w}}{30 \text{ km s}^{-1}} \right)^{4/3} \left(\frac{m_*}{0.3 M_\odot} \right)^{-2/3}, \quad (9)$$

and the Alfvén radius to be

$$\varpi_A = \varpi_0 \sqrt{\lambda} = 640 \text{ au}, \quad (10)$$

which is independent of $v_{p,w}$ or m_* . Note that we leave the jet velocity $v_{p,w}$ as a free parameter because even though the optical jet reaches about 300 km s^{-1} , the CS outflow may be entrained (toroidally) by the slower and less dense part of the jet which is not seen in optical lines.

Compared with other observations, such as Class 0 molecular jets (e.g., Lee et al. 2008, 2009; Choi et al. 2011), Class I H_2 jets (e.g., Chrysostomou et al. 2008), and optical T Tauri jets (e.g., Coffey et al. 2007), we have detected a similar rotational velocity at a much larger radius, and therefore higher specific angular momentum. Unlike prior observations, we believe here CS is not tracing the material directly launched from the disk but instead the entrained material. The detected velocity gradient could be evidence that the CS outflow is entrained not only poloidally but also toroidally by an MHD disk wind, and the derived footpoint radius suggests that this disk wind is launched from relatively large radii. We note that the measured specific angular momentum is only an upper limit because a similar velocity gradient with a smaller resolution beam will give a much smaller specific angular momentum. In fact, in the literature listed above, the reported specific angular momenta tend to be smaller with a higher angular resolution.

5. SUMMARY AND CONCLUSIONS

We present ALMA Cycle 1 observations of the HH 46/47 molecular outflow, combining the 12 m array, 7 m array, and single dish total power data. Compared with previous cycle 0 observations, the new observations have higher angular resolution ($1.''3$, nearly three times higher than before), ability to recover extended emission, and coverage of more molecular species, including ^{13}CO , C^{18}O , C^{17}O , CS, and C^{34}S . Our main conclusions are as follows.

1. We detect an extended component in the continuum emission, which is elongated with its major axis perpendicular to the outflow axis. Its morphology appears to be affected by the outflow. We conclude it traces a flattened envelope that is shaped by the bipolar outflow.
2. The new ^{13}CO and C^{18}O data allowed us to trace outflow material with a higher column density than ^{12}CO . They are only detected within about $1\text{--}2 \text{ km s}^{-1}$ from the cloud velocity, tracing the outflow to lower velocities than what is possible using only the ^{12}CO emission. Interestingly, the cavity wall of the redshifted outflow appears at very low velocities (as low as 0.2 km s^{-1}) in emission of these molecules.
3. We used the ^{13}CO and C^{18}O emission to correct for the CO optical depth and accurately estimated the mass, momentum, and kinetic energy of the outflow. Correcting for the ^{12}CO optical depth increases the estimated mass of the outflow by a factor of 8.5, the momentum by a factor of 4.9, and the kinetic energy by a factor of 2.4. Adding the slower material traced only by ^{13}CO and C^{18}O , there is

another factor of three increase in the mass estimate and 50% increase in the momentum estimate. Assuming $T_{\text{ex}} = 15$ K, the measured total mass of the outflow is $1.6 M_{\odot}$, the total momentum is $1.9 M_{\odot} \text{ km s}^{-1}$ (after correcting for inclination) and the total kinetic energy is 3.9×10^{43} erg. The estimated outflow mass and momentum are significantly higher than those previously reported from surveys of Class 0 and I outflows.

4. We derived the spatial distributions of the mass, momentum, and kinetic energy of the outflow. Despite the very different sizes and morphologies of the blueshifted and redshifted outflows, their energy distributions appear to be symmetric, and both are concentrated on the outflow cavity walls near the central source. Interestingly, even though the jet bow-shock entrainment is significant in the red lobe, more outflow energy is being deposited into the cloud at the base of the outflow cavity rather than close to the heads of the bow shocks.
5. By comparing the mass distributions of the outflow and the remaining core, we find that the molecular outflow is mainly composed of locally entrained core material, rather than being made of material that was entrained close to the source and then carried out to its current position. This indicates that the core material joins the outflow as the outflow cavity broadens. Based on such a scenario, we find that the outflow is capable of dispersing the core within the lifetime of the embedded phase of a typical low-mass protostar. We also estimated the current instantaneous core-to-star efficiency to be about 1/3, and the current average core-to-star efficiency to be 1/3 to 1/4, suggesting the outflow has already been significantly affecting the star formation efficiency.
6. The improved angular resolution and sensitivity allow us to see richer details of the outflow structure. Notably, we find that the outflow cavity wall of the redshifted outflow is composed of two or more layers of outflowing gas, which connect with different shocked regions along the outflow axis inside the cavity, suggesting that the outflow cavity wall is made of multiple shells entrained in a series of jet bow-shock events. For the blueshifted outflow, we showed the CO emission above about 6 km s^{-1} can be well fitted with the wide-angle wind entrainment model. However, we find evidence that both mechanisms are actually in action on both sides of the outflow, even though the mechanism that is more visible differs on the two sides due to the different environment of the outflow.
7. We identify a flattened structure around the central source perpendicular to the outflow axis in the ^{13}CO and C^{18}O (1–0) maps. The morphologies of this structure in the ^{13}CO and C^{18}O integrated images indicate that it is shaped by the outflow cavities. Comparison between the observed PV diagrams in both species and a simple analytic model suggest that the observed flattened structure can be explained by a collapsing envelope with rotation. We estimated an envelope infall rate of $3.2 \times 10^{-6} M_{\odot} \text{ yr}^{-1}$, which is enough to sustain the disk accretion rate suggested by the mass flux of the atomic jet. Higher angular resolution observations are needed to probe the transition from the infalling envelope to a rotationally supported disk and even higher resolution is needed to resolve the disks feeding each protostar in the binary system.

8. At outflow velocities from 1 to 4 km s^{-1} , the CS (2–1) emission traces a collimated structure along the outflow axis inside the outflow cavity. Its kinematics and spatial overlap with the ^{12}CO emission inside the cavity suggest that it is tracing jet-entrained material. We detect velocity gradients across its axis over its length. If this is due to the rotation of the outflow, the estimated specific angular momentum is about $1600 \text{ au km s}^{-1}$ and would also imply that the CS outflow is entrained, not only poloidally but also toroidally, by a disk wind launched from relatively large radii (60 au).

APPENDIX COLUMN DENSITY AND OPTICAL DEPTH CORRECTION

The radiative transfer equation in the form of radiation temperature is (e.g., Bourke et al. 1997)

$$T_R(v) = f [J_{\nu}(T_{\text{ex}}) - J_{\nu}(T_{\text{bg}})](1 - \exp(-\tau_v)), \quad (11)$$

where T_R is background-subtracted radiation temperature, T_{ex} is the excitation temperature (assumed constant along the line of sight), T_{bg} is the background temperature, f is the beam-filling factor, and

$$J_{\nu}(T) \equiv \frac{h\nu/k}{\exp\left(\frac{h\nu}{kT}\right) - 1}. \quad (12)$$

In LTE, the optical depth of a transition at velocity v relates to the column density of the molecule at that velocity by

$$\frac{dN}{dv} = \left(\frac{8\pi k \nu_{ul}^2}{hc^3 A_{ul} g_u} \right) Q_{\text{rot}}(T_{\text{ex}}) \exp\left(\frac{E_u}{kT_{\text{ex}}}\right) J_{\nu_{ul}}(T_{\text{ex}}) \tau_v, \quad (13)$$

where ν_{ul} is the frequency of the transition, A_{ul} is the Einstein A coefficient, E_u and g_u are the energy and degeneracy of the upper level, and Q_{rot} is the partition function ($Q_{\text{rot}}(T) = \sum_{J=0}^{\infty} g_J e^{-E_J/kT} = \sum_{J=0}^{\infty} (2J+1) e^{-B_0 J(J+1)/kT}$). We can estimate the column density from the measured intensity by combining Equations (11) and (13),

$$\frac{dN}{dv} = \left(\frac{8\pi k \nu_{ul}^2}{hc^3 A_{ul} g_u} \right) Q_{\text{rot}}(T_{\text{ex}}) \exp\left(\frac{E_u}{kT_{\text{ex}}}\right) \times \frac{J_{\nu_{ul}}(T_{\text{ex}})}{[J_{\nu}(T_{\text{ex}}) - J_{\nu}(T_{\text{bg}})]} \left(\frac{\tau_v}{1 - \exp(-\tau_v)} \right) \frac{T_R(v)}{f}. \quad (14)$$

Assuming $T_{\text{bg}} = 2.7$ K, $J(T_{\text{bg}})$ is insignificant compared to $J(T_{\text{ex}})$ for typical $T_{\text{ex}} > 10$ K at a frequency around 100 GHz. Also with a line width of $\lesssim 100 \text{ km s}^{-1}$, $J_{\nu}(T_{\text{ex}}) \approx J_{\nu_{ul}}(T_{\text{ex}})$. Therefore we have

$$\frac{dN}{dv} = \left(\frac{8\pi k \nu_{ul}^2}{hc^3 A_{ul} g_u} \right) Q_{\text{rot}}(T_{\text{ex}}) \times \exp\left(\frac{E_u}{kT_{\text{ex}}}\right) \left(\frac{\tau_v}{1 - \exp(-\tau_v)} \right) \frac{T_R(v)}{f}. \quad (15)$$

In the optically thin limit, $\tau \ll 1$, $\tau_v/(1 - \exp(-\tau_v)) \approx 1$, and

$$\frac{dN}{dv} = \left(\frac{8\pi k \nu_{ul}^2}{hc^3 A_{ul} g_u} \right) Q_{\text{rot}}(T_{\text{ex}}) \exp\left(\frac{E_u}{kT_{\text{ex}}}\right) \frac{T_R(v)}{f}. \quad (16)$$

Therefore

$$\frac{dN}{dv} = \frac{dN}{dv}|_{\text{thin}} F_\tau(v), \quad (17)$$

with the optical depth correction factor

$$F_\tau(v) \equiv \frac{\tau_v}{1 - \exp(-\tau_v)}. \quad (18)$$

For the ^{12}CO (1–0) line, we adopt $\nu_{ul} = 115.271$ GHz, $A_{ul} = 7.203 \times 10^{-8} \text{ s}^{-1}$, $g_u = 2J_u + 1 = 3$, $E_u = 5.53$ K, $B_0/k = 2.765$ K. We adopt $\nu_{ul} = 110.201$ GHz, $A_{ul} = 6.294 \times 10^{-8} \text{ s}^{-1}$, $g_u = 2J_u + 1 = 3$, $E_u = 5.29$ K, $B_0/k = 2.645$ K for the ^{13}CO (1–0) line, and $\nu_{ul} = 109.782$ GHz, $A_{ul} = 6.266 \times 10^{-8} \text{ s}^{-1}$, $g_u = 2J_u + 1 = 3$, $E_u = 5.27$ K, $B_0/k = 2.635$ K for the C^{18}O (1–0) line.

We estimate the optical depth correction factor F_τ following the method outlined by Dunham et al. (2014). Assuming ^{12}CO and ^{13}CO trace the same material and have the same T_{ex} and f , from Equation (11) we have

$$\frac{T_{R,12}(v)}{T_{R,13}(v)} = \frac{1 - \exp(-\tau_{v,12})}{1 - \exp(-\tau_{v,13})}, \quad (19)$$

where the subscripts 12 and 13 represent ^{12}CO and ^{13}CO , respectively. If ^{13}CO is optically thin ($\tau_{13} \ll 1$),

$$\frac{T_{R,12}(v)}{T_{R,13}(v)} = \frac{1 - \exp(-\tau_{v,12})}{\tau_{v,13}} \approx X_{12,13} \frac{1 - \exp(-\tau_{v,12})}{\tau_{v,12}}, \quad (20)$$

where $X_{12,13}$ is the abundance ratio between ^{12}CO and ^{13}CO . The last step is valid because the same transitions of the isotopologues at the same excitation temperature have very similar ν_{ul} , A_{ul} , E_u , g_u , $Q_{\text{rot}}(T_{\text{ex}})$ and then from Equation (13) we have

$$\frac{\tau_{12}}{\tau_{13}} \approx \frac{dN_{12}/dv}{dN_{13}/dv} = X_{12,13}. \quad (21)$$

Therefore the correction factor for the ^{12}CO optical depth can be estimated as

$$F_{\tau,12}(v) = X_{12,13} \frac{T_{R,13}(v)}{T_{R,12}(v)}, \quad (22)$$

assuming ^{13}CO is optically thin.

^{13}CO may not be optically thin at low velocities and we can use the less abundant and more optically thin isotopologue C^{18}O to correct the optical depth of ^{13}CO . In such a case, we have

$$F_{\tau,13}(v) = X_{13,18} \frac{T_{R,18}(v)}{T_{R,13}(v)}, \quad (23)$$

where the subscript 18 represents C^{18}O , $X_{13,18}$ is the abundance ratio between ^{13}CO and C^{18}O , and

$$F_{\tau,12}(v) = X_{12,13} \frac{T_{R,13}(v) F_{\tau,13}}{T_{R,12}(v)} = X_{12,13} \frac{T'_{R,13}(v)}{T_{R,12}(v)}, \quad (24)$$

where $T'_{R,12} \equiv T_{R,12}(v) F_{\tau,12}$ is optical-depth-corrected intensity. If the two isotopologues used for intensity ratios are both optically thin, we have $T_{R,12}/T'_{R,13} = X_{12,13}$ and $T_{R,13}/T_{R,18} = X_{13,18}$ as their upper limits, i.e., a lower limit of 1 for the optical depth correction factor F_τ . We note again that this method assumes

that these isotopologues trace the same material at the same excitation temperature under LTE conditions and have constant abundance ratios.

We thank the anonymous referee for helpful discussions. This paper makes use of the following ALMA data: ADS/JAO.ALMA #2012.1.00382.S. ALMA is a partnership of ESO (representing its member states), NSF (USA), and NINS (Japan), together with NRC (Canada), NSC and ASIAA (Taiwan), and KASI (Republic of Korea), in cooperation with the Republic of Chile. The Joint ALMA Observatory is operated by ESO, AUI/NRAO, and NAOJ. The National Radio Astronomy Observatory is a facility of the National Science Foundation operated under cooperative agreement by Associated Universities, Inc. YZ, DM and GG acknowledge support from the CONICYT Project PFB-06. SSRO acknowledges support from NSF grant AST-1510021.

REFERENCES

- Alves, J., Lombardi, M., & Lada, C. J. 2007, *A&A*, **462**, L17
- Anderson, J. M., Li, Z.-Y., Krasnopolsky, R., & Blandford, R. D. 2003, *ApJL*, **590**, 107
- Arce, H. G., & Goodman, A. A. 2001a, *ApJL*, **551**, L171
- Arce, H. G., & Goodman, A. A. 2001b, *ApJ*, **554**, 132
- Arce, H. G., Mardones, D., Corder, S. A., et al. 2013, *ApJ*, **774**, 39
- Arce, H. G., & Sargent, A. I. 2005, *ApJ*, **624**, 232
- Arce, H. G., & Sargent, A. I. 2006, *ApJ*, **646**, 1070
- Bourke, T. L., Garay, G., Lehtinen, K. K., et al. 1997, *ApJ*, **476**, 781
- Bradshaw, C., Offner, S. S. R., & Arce, H. G. 2015, *ApJ*, **802**, 86
- Cabrit, S., Ferreira, J., & Raga, A. C. 1999, *A&A*, **343**, L61
- Chernin, L. M., & Masson, C. R. 1991, *ApJL*, **382**, L93
- Choi, M., Kang, M., & Tatematsu, K. 2011, *ApJ*, **728**, 34
- Chrysostomou, A., Bacciotti, F., Nisini, B., et al. 2008, *A&A*, **482**, 575
- Coffey, D., Bacciotti, F., Ray, T. P., Eisloeffel, J., & Woitas, J. 2007, *ApJ*, **663**, 350
- Curtis, E. I., Richer, J. S., Swift, J. J., & Williams, J. P. 2010, *MNRAS*, **408**, 1516
- Downes, T. P., & Cabrit, S. 2007, *A&A*, **471**, 873
- Dunham, M. M., Allen, L. E., Evans, N. J., et al. 2015, *ApJS*, **220**, 11
- Dunham, M. M., Arce, H. G., Mardones, D., et al. 2014, *ApJ*, **783**, 29
- Dunham, M. M., Stutz, A. M., Allen, L. E., et al. 2014, in Protostars and Planets VI, ed. H. Beuther et al. (Tucson, AZ: Univ. Arizona Press), 195
- Eisloeffel, J., Davis, C. J., Ray, T. P., & Mundt, R. 1994, *ApJL*, **422**, L91
- Eisloeffel, J., & Mundt, R. 1994, *A&A*, **284**, 530
- Ellerbroek, L. E., Podio, L., Kaper, L., et al. 2013, *A&A*, **551**, 5
- Federrath, C., Schrön, M., Banerjee, R., & Klessen, R. S. 2014, *ApJ*, **790**, 128
- Ferreira, J., Dougados, C., & Cabrit, S. 2006, *A&A*, **453**, 785
- Fuller, G. A., & Ladd, E. F. 2002, *ApJ*, **573**, 699
- Harsono, D., Jørgensen, J. K., van Dishoeck, E. F., et al. 2014, *A&A*, **562**, 77
- Hartigan, P., Heathcote, S., Morse, J. A., Reipurth, B., & Bally, J. 2005, *AJ*, **130**, 2197
- Hartigan, P., Morese, J. A., & Raymond, J. 1994, *ApJ*, **436**, 125
- Hatchell, J., Fuller, G. A., & Richer, J. S. 2007, *A&A*, **472**, 187
- Langer, W. D., & Penzias, A. A. 1993, *ApJ*, **408**, 539
- Lee, C.-F., Hirano, N., Palau, A., et al. 2009, *ApJ*, **699**, 1584
- Lee, C.-F., Hirano, N., Zhang, Q., et al. 2015, *ApJL*, **805**, 186
- Lee, C.-F., Ho, P. T. P., Beuther, H., et al. 2006, *ApJ*, **639**, 292
- Lee, C.-F., Ho, P. T. P., Bourke, T. L., et al. 2008, *ApJ*, **685**, 1026
- Lee, C.-F., Mundy, L. G., Reipurth, B., Ostriker, E. C., & Stone, J. M. 2000, *ApJ*, **542**, 925
- Lee, C.-F., Stone, J. M., Ostriker, E. C., & Mundy, L. G. 2001, *ApJ*, **557**, 429
- Li, Z.-Y., & Shu, F. H. 1996, *ApJ*, **472**, 211
- Mardones, D., Myers, P. C., Tafalla, M., et al. 1997, *ApJ*, **489**, 719
- Matzner, C. D., & McKee, C. F. 2000, *ApJ*, **545**, 364
- Micenko, M., Davis, C. J., Ray, T. P., Eisloeffel, J., & Shetrone, M. D. 1998, *ApJL*, **494**, L227
- Motte, F., & André, P. 2001, *A&A*, **365**, 440
- Myers, P. C. 2008, *ApJ*, **687**, 340
- Noriega-Crespo, A., Moro-Martí, A., Carey, S., et al. 2004, *ApJS*, **154**, 402
- Noriega-Crespo, A., & Raga, A. C. 2012, *ApJ*, **750**, 101
- Offner, S. S. R., & Arce, H. G. 2014, *ApJ*, **784**, 61

- Offner, S. S. R., Clark, P. C., Hennebelle, P., et al. 2014, in *Protostars and Planets VI*, ed. H. Beuther et al. (Tucson, AZ: Univ. Arizona Press), 53
- Offner, S. S. R., Lee, E. J., Goodman, A. A., & Arce, H. 2011, *ApJ*, 743, 91
- Ohashi, N., Hayashi, M., Ho, P. T. P., & Momose, M. 1997, *ApJ*, 475, 211
- Olberg, M., Reipurth, B., & Booth, R. S. 1992, *A&A*, 259, 252
- Ossenkopf, V., & Henning, T. 1994, *A&A*, 291, 943
- Raga, A., & Cabrit, S. 1993, *A&A*, 278, 267
- Reipurth, B. 1989, in *Proc. ESO Workshop on Low Mass Star Formation and Pre-Main Sequence Objects*, ed. B. Reipurth, (Garching: ESO), 247
- Reipurth, B. 2000, *AJ*, 120, 1449
- Reipurth, B., & Heathcote, S. 1991, *A&A*, 246, 511
- Richer, J. S., Shepherd, D. S., Cabrit, S., Bachiller, R., & Churchwell, E. 2000, in *Protostars and Planets IV*, ed. V. Mannings, A. P. Boss, & S. S. Russell, (Tucson, AZ: Univ. Arizona Press), 867
- Sakai, N., Sakai, T., Hirota, T., et al. 2014, *Natur*, 507, 78
- Schwartz, R. D. 1977, *ApJL*, 212, L25
- Shang, H., Allen, A., Li, Z.-Y., et al. 2006, *ApJ*, 649, 845
- Smith, M. D., Suttner, G., & Yorke, H. W. 1997, *A&A*, 323, 223
- Stanke, T., McCaughrean, M. J., & Zinnecker, H. 1999, *A&A*, 350, L43
- Su, Y.-N., Zhang, Q., & Lim, J. 2004, *ApJ*, 604, 258
- Tafalla, M., & Myers, P. C. 1997, *ApJ*, 491, 653
- van Kempen, T. A., Kristensen, L. E., Herczeg, G. J., et al. 2010, *A&A*, 518, L121
- van Kempen, T. A., van Dishoeck, E. F., Güsten, R., et al. 2009, *A&A*, 501, 633
- Velusamy, T., & Langer, W. D. 1998, *Natur*, 392, 685
- Velusamy, T., Langer, W. D., & Marsh, K. A. 2007, *ApJL*, 668, L159
- Wampfler, S. F., Herczeg, G. J., Bruderer, S., et al. 2010, *A&A*, 521, L36
- Wilson, T. L., & Matteucci, F. 1992, *A&ARv*, 4, 1
- Yen, H.-W., Takakuwa, S., Ohashi, N., & Ho, P. T. P. 2013, *ApJ*, 772, 22
- Zhang, Y., & Tan, J. C. 2015, *ApJL*, 802, L15